



Cassini–VIMS observations of Saturn's main rings: I. Spectral properties and temperature radial profiles variability with phase angle and elevation



G. Filacchione ^{a,*}, M. Ciarniello ^a, F. Capaccioni ^a, R.N. Clark ^b, P.D. Nicholson ^c, M.M. Hedman ^d, J.N. Cuzzi ^e, D.P. Cruikshank ^e, C.M. Dalle Ore ^e, R.H. Brown ^f, P. Cerroni ^a, N. Altobelli ^g, L.J. Spilker ^h

^a INAF-IAPS, Istituto di Astrofisica e Planetologia Spaziali, Area di Ricerca di Tor Vergata, via del Fosso del Cavaliere, 100, 00133 Rome, Italy

^b US Geological Survey, Federal Center, Denver, CO 80228, USA

^c Cornell University, Astronomy Department, 418 Space Sciences Building, Ithaca, NY 14853, USA

^d Department of Physics, University of Idaho, Moscow, ID 83844-0903, USA

^e NASA Ames Research Center, Moffett Field, CA 94035-1000, USA

^f Lunar Planetary Laboratory, University of Arizona, Kuiper Space Sciences 431A, Tucson, AZ 85721, USA

^g ESA/ESAC, Villanueva de la Canada, Spain

^h Jet Propulsion Laboratory, California Institute of Technology, Pasadena, CA 91109, USA

ARTICLE INFO

Article history:

Received 16 January 2014

Revised 5 May 2014

Accepted 2 June 2014

Available online 30 June 2014

Keywords:

Saturn, rings

Spectroscopy

Ices

ABSTRACT

The spectral properties and thermal behavior of Saturn's rings are determined from a dataset of ten radial mosaics acquired by Cassini–VIMS (Visual and Infrared Mapping Spectrometer) between October 29th 2004 and January 27th 2010 with phase angle ranging between 5.7° and 132.4° and elevation angles between –23.5° and 2.6°. These observations, after reduction to spectrograms, e.g. 2D arrays containing the VIS–IR (0.35–5.1 μm) spectral information versus radial distance from Saturn (from 73.500 to 141.375 km, 400 km/bin), allow us to compare the derived spectral and thermal properties of the ring particles on a common reference. *Spectral properties*: rings spectra are characterized by an intense reddening at visible wavelengths while they maintain a strong similarity with water ice in the infrared domain. Significant changes in VIS reddening, water ice abundance and grain sizes are observed across different radial regions resulting in correlation with optical depth and local structures. The availability of observations taken at very different phase angles allows us to examine spectrophotometric properties of the ring's particles. When observed at high phase angles, a remarkable increase of visible reddening and water ice band depths is found, probably as a consequence of the presence of a red-colored contaminant intimately mixed within water ice grains and of multiple scattering. At low phases the analysis of the 3.2–3.6 μm range shows faint spectral signatures at 3.42–3.52 μm which are compatible with the CH₂ aliphatic stretch. The 3.29 μm PAH aromatic stretch absorption is not clearly detectable on this dataset. VIMS results indicate that ring particles contain about 90–95% water ice while the remaining 5–10% is consistent with different contaminants like amorphous carbon or tholins. However, we cannot exclude the presence of nanophase iron or hematite produced by iron oxidation in the rings tenuous oxygen atmosphere, intimately mixed with the ice grains. Greater pollution caused by meteoritic material is seen in the C ring and Cassini division while the low levels of aliphatic material observed by VIMS in the A and B rings particles are an evidence that they are pristine. *Thermal properties*: the ring-particles' temperature is retrieved by fitting the spectral position of the 3.6 μm continuum peak observed on reflectance spectra: in case of pure water ice the position of the peak, as measured in laboratory, shifts towards shorter wavelengths when temperature decreases, moving from about 3.65 μm at 123 K to about 3.55 μm at 88 K. When applied to VIMS rings observations, this method allows us to infer the average temperature across ring regions sampled through 400 km-wide radial bins. Comparing VIMS temperature radial profiles with similar CIRS measurements acquired at the same time we have found a substantial agreement between the two instruments' results across the A and B rings. In general VIMS measures higher temperatures than CIRS across C ring and Cassini division as a consequence of the lower optical depth and the resulting pollution that creates a deviation from pure water ice composition of these regions. VIMS results point out that across C ring and CD the 3.6 μm peak wavelength is always higher than across B and A rings and

* Corresponding author.

E-mail address: gianrico.filacchione@iaps.inaf.it (G. Filacchione).

therefore C ring and CD are warmer than A and B rings. VIMS observations allow us to investigate also diurnal and seasonal effects: comparing antisolar and subsolar ansae observations we have measured higher temperature on the latter. As the solar elevation angle decreases to 0° (equinox), the peak's position shifts at shorter wavelengths because ring's particles becomes colder. Merging multi-wavelength data sets allow us to test different thermal models, combining the effects of particle albedo, regolith composition, grain size and thermal properties with the ring structures.

© 2014 Elsevier Inc. All rights reserved.

1. Introduction

Among the planets of the Solar System, Saturn has the most prominent and complex ring system which spans more than 62,000 km from 74,658 km (inner C ring) to 136,780 km (outer A ring). The composition of Saturn's ring particles was first characterized thanks to telescopic infrared observations in the '70s (Pilcher et al., 1970; Lebofsky et al., 1970; Kuiper et al., 1970), which showed the rings were composed mainly of water ice. Afterward, Voyager observations at visible wavelengths pointed out that the optically thick A and B rings have redder spectra than the darker and optically thin C ring and Cassini division (Smith et al., 1981, 1982). Moreover, the large surface/volume ratio of the disk results in a highly efficient collecting area to capture the meteoroid flux, whose ejecta are then incorporated in the rings particles because of their low velocities (Cuzzi and Durisen, 1990). This information drove the development of the "ballistic transport model" by Cuzzi and Estrada (1998) in which the constant infall of meteoritic material on the ring disk, accumulating in the optically thin regions induces a pollution of the icy particles orbiting within these zones resulting in darker and more neutral-colored reflectance spectra. This scenario has prompted further efforts to model ring visible-infrared reflectance spectra acquired from Earth (Poulet et al., 2003) using mixtures of water ice and different chromophores, like tholins or amorphous carbon. Also HST observations were frequently used to perform photometry studies of the main rings as function of phase and opening angle between 255 and 1042 nm (Cuzzi et al., 2002) and to characterize the ring's azimuthal brightness asymmetry (French et al., 2007).

In the last decade Saturn ring's composition studies further continued thanks to the continuous stream of VIS-IR data returned by VIMS, the Visual and Infrared Mapping Spectrometer (Brown et al., 2004), onboard the Cassini mission. A review about rings' composition from VIMS and the other Cassini's payloads can be found in Cuzzi et al. (2009, 2010). Several analyses conducted on VIMS data have pointed out the spectral variability of the particles across different rings regions (Nicholson et al., 2008) but to date, despite the high performances of VIMS, there has been no detection of diagnostic spectral features which could help to identify the non-icy component, with the only exception of the reddening affecting the visible part of the spectrum (Cuzzi et al., 2009; Filacchione et al., 2012).

Different approaches have been exploited to characterize composition and model visible-infrared light-scattering properties of the regolith coating the rings particles. Shkuratov et al. (1999) geometrical optics model was applied by Poulet and Cuzzi (2001) to infer ring particles composition from ground-based observations by deriving an intimate mixing of water ice particles with few percent of embedded tholin and amorphous carbon particles. An alternative method, based on brightness ratios described in the same Shkuratov et al. (1999) paper, allows us to retrieve the spatial distribution of two different contaminants populations, the first absorbing across a wide spectral visible-infrared range, the second that absorbs only at short visible wavelengths (Hedman et al., 2013). A different approach is based on Monte Carlo raytracing

simulations applied to particulate media of given composition, grain size distribution and filling factor (Ciarniello et al., 2013, 2014). This method allows a better characterization of the grains' composition by using Hapke (1993) theory in the cases in which multiple scattering among rings particles is not negligible. In fact even if single scattered light dominates the total power reflected by the rings plane, the inter-particle (multiple) scattering fraction produces a dependence of the spectral features on observation geometry, in particular phase angle, at least for the more dense regions of the rings (Ciarniello et al., 2012). Other very different approaches were developed to simulate VIMS observations: in order to consider the role played by ring particles' roughness and irregular surfaces (Cuzzi et al., 1984; Vahidinia et al., 2011) have applied light scattering models based on Mie and discrete dipole approximations to F ring VIMS spectra. Alternatively, a radiative transfer code was used by D'Aversa et al. (2010) to model spokes' spectra observed in 2008 by VIMS on the B ring.

The origin of the UV absorber (Bradley et al., 2013) is largely debated in the ring community because the nature and distribution of this chromophore has important implications on the age and formation mechanisms of Saturn's rings. As reported by Filacchione et al. (2013) VIMS has found a marked uniformity in the distribution of the abundance of water ice across the saturnian system while chromophores are much more concentrated in the rings particles and on the outermost satellites (Rhea, Hyperion, Iapetus and Phoebe). At the same time a reduction of the red material on the satellites surfaces orbiting within the E ring environment is observed as a consequence of the layering of fine water ice particles sprayed by Enceladus plumes (Porco et al., 2006) released from the "tiger stripes" features on the south polar region (Brown et al., 2006; Jaumann et al., 2006). Apart the meteoritic infall, both Phoebe's ring discovered by Verbiscer et al. (2009), and the outer irregular satellites (Tosi et al., 2010) are possible sources of exogenous dark material polluting the external saturnian system and driving the compositional gradients observed on the surfaces of the outer satellites (Filacchione et al., 2013): the accumulation of dark material on Iapetus' leading hemisphere is the most evident consequence of these processes as reported by Clark et al. (2012) and Dalle Ore et al. (2012). However, the main ring system is currently unaffected by similar contamination because the flux of dust particles coming from Phoebe's ring and outer irregular satellites vanishes between Iapetus' and Hyperion's orbits according to dynamical simulations performed by Tamayo et al. (2011).

Rings' particle composition and regolith properties can be inferred through the comparison of VIMS observations with laboratory and synthetic spectra of analog icy materials. For each ring region it is essential to process as many observations as possible taken at different illumination and viewing geometries, in order to decouple the photometric phase response from spectral analysis. As described in Hapke (1993), when phase changes the reflectance spectra are influenced in different ways by single and multiple scattering which occur among the regolith grains covering the surface of a given ring particle: at low phase in fact multiple scattering influences the continuum and the wings of the absorption band

where the single scattering albedo is high. At the same time single scattering dominates within the band where albedo is low and consequently photons are immediately absorbed by the medium. When phase increases the single scattering prevails over multiple scattering across the band. Finally, at very high phases, e.g. in forward scattering viewing geometry, multiple scattering becomes the dominant process, especially for a medium composed by particles having a size larger than the wavelength. The consequences of these effects are verified on many spectral indicators – e.g. visible spectral slopes and infrared band depths – discussed later in Section 3.

Observations taken above rings' regions with phase between 20° and 40° are preferentially employed to retrieve the composition. In these cases, in fact, the complications induced by multiple and forward scattering are minimized. According to Cuzzi et al. (2009) ring particles are composed of pure crystalline water ice up to 90–95%. The strong reddening characterizing ring spectra at wavelengths lower than 0.55 μm indicates the presence of a non-icy component that must represent the remaining few percent by mass. Any absorption features of CO₂, CH₄, NH₃ ices and silicates are not detected on VIMS spectra (Cuzzi et al., 2010). As discussed by Cuzzi et al. (2009) and Clark et al. (2012) a few percent of nano-phase iron or hematite particles, a byproduct of iron oxidation in the tenuous oxygen-rich atmosphere around rings, mixed in water ice can reproduce the average rings optical properties causing a strong UV absorption without introducing alteration to water ice spectral reflectance in the 1–5 μm range. VIMS data point out that rings spectra are strongly correlated with the local optical depth and surface mass density while spectral changes along the radial axis are probably due to regolith grain size variation more than compositional variations (Nicholson et al., 2008). As a general rule C ring and Cassini division are more contaminated by non-icy end-members than the A and B rings (Cuzzi and Estrada, 1998). Furthermore, the water ice band depths are strongly correlated with the visual reddening, implying that the UV absorber must be intimately mixed within ice particles (Cuzzi et al., 2009; Filacchione et al., 2012; Hedman et al., 2013).

The contaminants distribution appears correlated with the rings temperature radial variation, where C ring and Cassini division particles are warmer than A and B ring particles. This property, observed for the first time on Voyager's IRIS infrared spectrometer data (Hanel et al., 1982), is a consequence of the low albedo particles in C ring and Cassini division where non-icy materials accumulate. Moreover, C ring and Cassini division higher temperature is caused by the reduced mutual shadowing among particles as a consequence of the low optical depth (Spilker et al., 2003). Conversely, lower temperatures are typical of the A-B ring particles whose composition is dominated by water ice. Cassini's CIRS, Composite InfraRed Spectrometer (Kunde, 1996; Flasar et al., 2004), is able to derive ring particles temperature and filling factor from spectral radiance data between 100 and 400 cm⁻¹ (100–25 μm) (Spilker et al., 2006). Radial and azimuthal distributions of these quantities measured with solar elevation angle between -23° and -13.4° are discussed in Altobelli et al. (2008) and Leyrat et al. (2008), respectively. At equinox, when the solar elevation angle approaches 0°, the ring plane is no longer directly illuminated by the Sun. In this geometry, ring particles receive the saturnshine and Saturn's thermal flux on dayside part of the ring orbit while the Saturn's thermal emission at T = 95 K is radiated on the nightside. As a consequence of the continuous reduction of the direct solar flux during the season from solstice to equinox, ring particles cool down: according to Spilker et al. (2013) the ring temperatures measured by CIRS at equinox were 55–75 K on C ring, 45–60 K on B ring, 45–58 K on Cassini division and 43–52 K on A ring. Based on these temperature measurements, different thermophysical models were built: the monolayer ring model

(Ferrari and Leyrat, 2006) can reproduce the observed temperature variations in the C ring at different local times; the temperatures of the B and C rings can be successfully simulated also by the multi-layer model (Morishima et al., 2009) which, however, fails to simulate A ring's temperature.

With this paper we are starting a study of the spectrophotometric properties of the rings particles using a common VIMS dataset, consisting in ten radial mosaics acquired between October 29th 2004 and January 27th 2010 with phase angle ranging between 5.7° and 132.4° and elevation angle between -23.5° and 2.6°. In this paper (I) we report about Saturn's rings spectral properties and temperature radial profiles variability as function of phase angle and elevation angle. Section 2 contains a description of the VIMS observations, including a description of the method applied to derive rings spectrograms; rings average spectral properties, signal to noise ratio and estimation of the error affecting VIMS measurements are discussed. In Section 3 we describe the radial profiles derived for several spectral indicators we have selected to study the rings variability, including the I/F(0.55 μm), the two spectral slopes S_{0.35–0.55} and S_{0.55–0.95}, the water ice 1.5–2.0 μm band depth and the ratio I/F(3.6) / I/F(1.8). A discussion about the variability of these indicators induced by phase angle is given in Section 4. Section 5 describes the temperature-dependent 3.6 μm continuum peak position we have used as a proxy to infer ring particles temperature through calibration with laboratory data. VIMS results are compared with CIRS temperatures measured at the same time. In Section 6 we report about the detection of faint absorption features in the 3.2–3.5 μm spectral range associated with organic material in the aliphatic form. Finally, in Section 7 a summary of the main findings is given.

2. Observations and data analysis

2.1. Observations

The VIMS instrument is based on two co-aligned imaging spectrometers (VIMS-V and VIMS-IR) observing the same field of view (1.83°) in two spectral ranges (Brown et al., 2004). The VIMS-V channel operates in the 0.35–1.05 μm range using 96 spectral channels, a spectral sampling of Δλ = 7.3 nm/band and spatial resolutions of 500 (nominal mode) or 166 (high resolution mode) μrad/pixel; the VIMS-IR channel works in the 0.885–5.1 μm spectral range resolving it in 256 bands with a spectral sampling of Δλ = 16.6 nm/band and spatial resolutions of 500 (nominal mode) or 250 × 500 (high resolution mode) μrad/pixel. For the sake of brevity we do not repeat here a full description of the VIMS data calibration process nor of the VIMS data format which were already addressed in McCord et al. (2004), Coradini et al. (2004), Filacchione (2006, 2007, 2012), Clark et al. (2008, 2012) and Cruikshank et al. (2010). In this work we have selected and analyzed a dataset consisting of ten ring radial mosaics from which the average spectral characteristics of the ring system along the radial axis are retrieved. Details about VIMS mosaics, including observation geometries, are reported in Table 1.

All the observations were performed in lit-side geometry with phase angles, measured in the middle B ring (at about r = 104,000 km from Saturn), running between 5.7° and 132.4° and solar elevation angle between -23.5° and 2.6°. Since VIMS-V and VIMS-IR can be independently commanded to operate with different spatial resolutions (nominal and high), the resulting scale on the hyperspectral images changes accordingly: in nominal-resolution mode both spectral channels have a square IFOV (Instantaneous Field of View) of 500 × 500 μrad; in high-resolution mode the VIS channel has a square IFOV of 166 × 166 μrad while the IR channel IFOV is a rectangle of 250 × 500 μrad. This means that

Table 1

Summary of VIMS ring dataset. Roman numbers are used to identify datasets in the following text and figures. A and S indicate antisolar and solar ansa observations, respectively. VIMS nominal (N) and high spatial resolution (H) modes are reported in the fifth column. B and B_0 correspond to the spacecraft and solar elevation angles, respectively.

Observation number and sequence	Ansa	Middle time (UTC)	Int. time VIS-IR (ms)	Res. VIS-IR	S/C-Saturn distance (km)	B ring phase (deg)	B (deg)	B_0 (deg)	SubS/C lon (deg)	Number VIS-IR spectra
I – S05-LATPHASE001	A	2004-303T18:26	5120 – 80	N-N	983287	132.4	-10.4	-23.5	113.2	2200
II – S10-SUBML07LP001	S	2005-104T07:57	10000 – 160	H-H	620713	30.7	-7.5	-22.0	23.1	8640
III – S10-LATPHASE001	A	2005-120T10:37	5120 – 80	N-H	1515808	33.3	-19.3	-21.9	145.2	2,634
IV – S11-RDHRCOMP001	A	2005-141T00:48	3840 – 80	N-H	307587	29.2	-12.4	-21.6	194.0	8192
V – S13-LATPHASE001	S	2005-230T22:07	5120 – 80	H-H	1091785	32.6	-21.3	-20.7	67.2	18,240
VI – S13-LATPHASE001	A	2005-231T01:18	5120 – 80	H-H	1029324	20.2	-21.5	-20.7	172.3	17,950
VII – S28-PHOTLT007	S	2007-049T14:48	7680 – 80	H-H	974535	96.0	-49.3	-13.7	43.7	13,630
VIII – S36-SUBML001	S	2007-353T21:35	10000 – 160	H-H	638829	38.8	-10.7	-9.2	67.9	10,340
IX – S36-SUBML001	A	2007-354T00:03	10000 – 160	H-H	703801	19.2	-9.0	-9.2	147.5	11,320
X – S57-LOWPHASE001	A	2010-027T09:07	5120 – 80	N-H	287325	5.7	4.4	2.6	10.5	8420

only when the two channels are both in nominal-resolution the resulting images have compatible scales. As reported in Table 1, only observation (I) was acquired with both channels operating in nominal-resolution mode, resulting in a spatial resolution of 490 km/pixel along the radial direction from a distance of 983,287 km. For the remaining observations the radial spatial resolution changes between the VIS and IR channels. Taking into account the combination between distance and instrumental modes, the highest spatial resolution achievable from this dataset can be evaluated: for the VIS channel it is 103 km/pixel, occurring during observation (II) acquired in high-resolution mode; for the IR channel it is 144×72 km/pixel for high-resolution mode observation (X). As far as the azimuthal spatial resolution is concerned, we must remember that since the ring observations are obtained with oblique viewing geometries – see the B angle, e.g. the spacecraft (S/C) opening angle values reported in Table 1 – the resulting images have different spatial scale across the FOV, resulting in better spatial resolution on the portion of the ring plane closer to the spacecraft and worse on the farther. This effect is particularly evident for observations obtained when the spacecraft was at equatorial latitudes (small opening angles) like in (II)–(X) while is negligible when the spacecraft was at much higher latitudes like in (VII).

The ring radial mosaics considered in this work were acquired by VIMS operating in imaging mode, e.g. using the internal scan mirrors mechanisms to build a bi-dimensional image, while the Cassini spacecraft was staring in inertial mode at fixed locations placed through the ring's ansa. Each station of the mosaic was commanded with an angular offset smaller than one instrumental FOV in order to guarantee an overlap between consecutive acquisitions. In this way it was possible to avoid radial gaps and obtain a better spatial reconstruction of the mosaics. Furthermore, each station was observed for a sufficient period of time to allow VIMS to complete the acquisitions of the lines necessary to complete a single hyperspectral cube. Typically, during these observations the Cassini spacecraft was oriented in such a way to maintain VIMS slit's direction tangential to the ring's ansa radial direction with the scan occurring perpendicular to it. The views of the rings during each mosaic are shown in Fig. 1: in these renderings the nominal VIMS FOV (64×64 mrad) is indicated by the orange square, with the slit direction along the horizontal direction and the scan direction along the vertical direction. Moreover subsolar (S) or

antisolar (A) ansa viewed by VIMS are specified in Table 1: in general observations taken on the antisolar ansa are preferential to retrieve spectral information because this minimizes the saturn-shine contamination on the rings. At the same time antisolar ansa observations offer better signal to noise conditions than the solar ansa ones because the phase angle is lower on the former than on the latter. We have verified this to be the case by considering two data sets (V)–(VI) and (VIII)–(IX) for which two scans of the two ansa at nearly the same viewing geometry are available.

Each VIMS hyperspectral cube is calibrated according to the method already discussed in Filacchione et al. (2012) which for brevity we do not repeat here. Particular care was devoted in this case to reduce the readout and electronic offset which characterize the response of the VIMS-VIS channel's CCD which is often the case for the rings at short wavelengths. These effects become particularly evident in low signal to noise conditions which, in case of the rings occur often in the blue spectral range. For each mosaic we have subtracted pixel by pixel a deep-sky observation, taken far from rings before or after the acquisition of the science data while maintaining the same instrument's operative mode and integration time. This method, used in synergy with a despiking algorithm, allows us to greatly improve the quality of the VIS channel data (Filacchione et al., 2007). In some cases the IR channel spectra are affected by calibration residuals across the three order sorting filter gaps placed at 1.65, 2.9, 3.9 μm as well as by some hot IR pixels, in particular at 1.22 and 4.74 μm wavelengths. Finally, also IR spectra are processed with a standard despiking filter to remove out of statistics and negative pixels.

2.2. Radial spectrograms

Since one of the primary goals of this study is the comparison of the spectral properties of the different ring regions observed from very different geometries we need a tool able to allow us to perform such comparisons. For this reason we have built radial spectrograms which place the reflectance spectra of each VIMS pixel on a common spatial reference. This method is the same as used before to reduce rings IR observations (Nicholson et al., 2008; Hedman et al., 2013). We have built VIS-IR radial spectrograms for each mosaic reported in Table 1 according to the method already discussed in Filacchione et al. (2012) which allows to merge together the VIMS-VIS and IR channels data in a 2D array

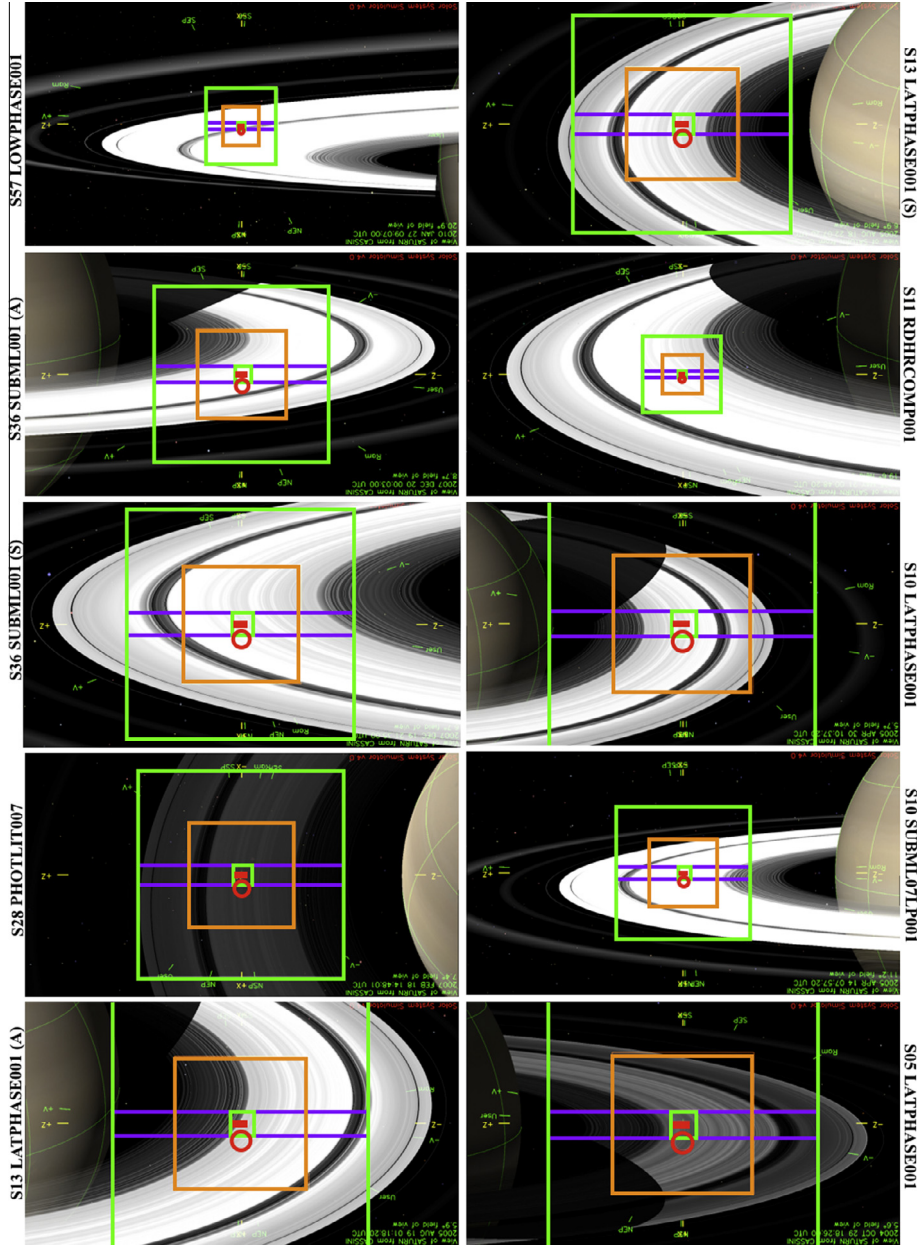


Fig. 1. Renderings of the VIMS views during mosaics acquisitions (from iDigit, by David Seal, NASA-JPL). Left column, from top to bottom: (X), (IX), (VIII), (VII), (VI). Right column, from top to bottom: (V), (IV), (III), (II), (I). The orange square indicates the VIMS 64×64 mrad nominal FOV. The two small and large green squares correspond to the ISS NAC and WAC FOVs, respectively. The magenta rectangle indicates the UVIS FOV and finally the red circle and rectangle the two CIRS FOVs. (For interpretation of the references to color in this figure legend, the reader is referred to the web version of this article.)

containing the $0.35\text{--}5.1\,\mu\text{m}$ spectral information sorted according to the radial distance from Saturn (from 73,500 to 141,375 km at 400 km/bin).

As an example, we show the radial spectrogram derived from observation (VIII) in Fig. 2. Moving away from Saturn is possible to observe:

- the faint C ring, extending between 74,658 and 91,975 km, has an optical depth of about 0.05 in the inner part which increases to about 0.35 in the outer region where the Maxwell gap (87,523 km) is barely resolved at 400 km resolution. The 17,317 km total width of the C ring is sampled by about 43 bins on VIMS spectrograms;
- with an optical depth ranging between 0.4 and >2.5 , the B ring is the most massive and reflective region; it spans between 91,975 and 117,507 km including four regions along the radius

named B1–B2–B3–B4 according to the nomenclature given in Marouf et al. (2006). The inner part of the B ring, named B1 ($92,000 < r < 99,000$ km) is characterized by a lower optical depth and smaller reflectance than the B2 region ($99,000 < r < 104,500$ km), where significant variations both in color and in water ice band depth are seen. The outer regions B3–B4 are the brightest and reddest regions of the system. On VIMS spectrograms the B ring spans across about 64 bins;

- the faint Cassini division (CD) extends to a width of 5000 km between 117,507 and 122,340 km. The narrow Huygens gap is localized close to the inner edge at 118,005 km. CD is resolved with about 12 radial bins on VIMS spectrograms;
- an optical depth of 0.4–1.0 characterizes the outermost A ring which is placed between 122,340 and 136,780 km (36 radial bins). The 300 km-wide Encke gap (133,410–133,740 km) is resolved in the spectrograms.

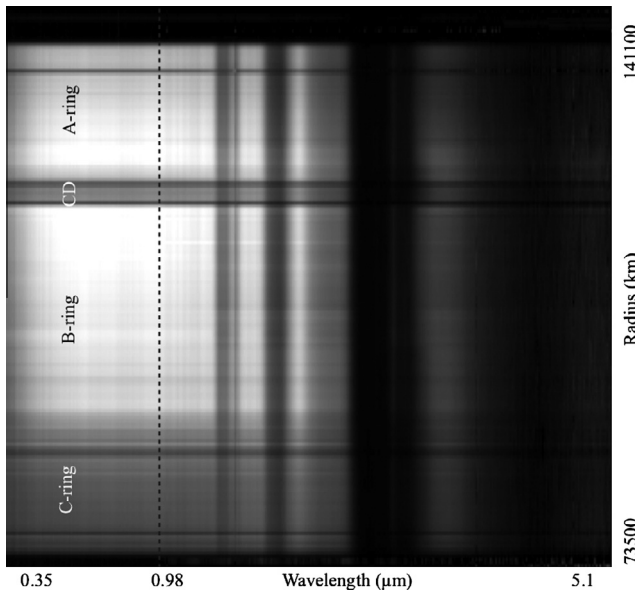


Fig. 2. Example of rings spectrogram as derived from observation VIII. The radial direction is shown along the vertical axis, while the horizontal axis corresponds to spectral dispersion from 0.35 to 0.98 (VIMS-V) to 0.98–5.1 μm (VIMS-IR). Rings regions can be recognized along the radial axis where C, B, A rings and CD (Cassini division) are indicated.

The corresponding average rings reflectance spectra are shown in Fig. 3: at visible wavelengths Saturn's rings reflectance spectra are characterized by a steep slope between 0.35 and 0.55 μm range. This feature is caused by the presence of a still unknown UV absorber material mixed within water ice particles. The reddening effect is more evident across the regions having higher optical depth, like A and B rings, while is less pronounced across C ring and CD where the optical depth is much lower. In the 0.55–0.98 μm range A–B ring spectra appear flat while C and CD are both moderately red. In the infrared range water ice dominates across the entire ring system showing absorption bands at 1.05, 1.25, 1.5, 2.05, 3.0 μm which are comparable in strength to the values

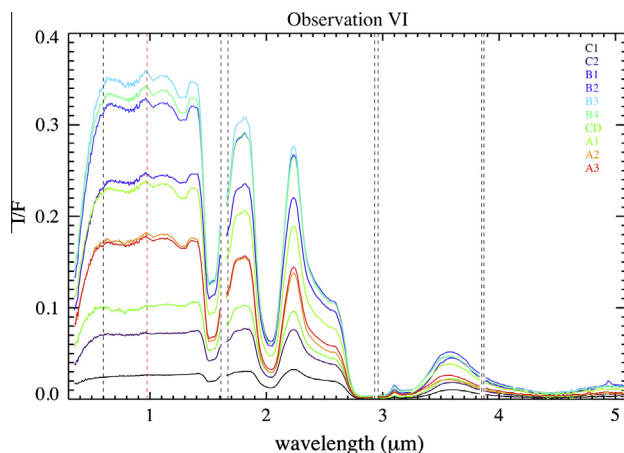


Fig. 3. Average reflectance spectra for different ring regions: C1 ($74,658 \leq r \leq 87,523$ km), C2 ($87,523 \leq r \leq 91,795$ km), B1 ($91,795 \leq r \leq 99,000$ km), B2 ($99,000 \leq r \leq 104,500$ km), B3 ($104,500 \leq r \leq 110,000$ km), B4 ($110,000 \leq r \leq 117,500$ km), CD ($117,500 \leq r \leq 122,340$ km), A1 ($122,340 \leq r \leq 127,000$ km), A2 ($127,000 \leq r \leq 133,575$ km), A3 ($133,575 \leq r \leq 136,780$ km). Spectral sampling is 7.3 nm/band between 0.35 and 0.98 μm (VIMS-V range) and 16.5 nm/band between 0.98 and 5.1 μm (VIMS-IR range). VIS and IR bridging wavelength at 0.98 μm is indicated by the vertical red dash line. VIMS order sorting filters junctions are indicated by vertical black dash lines.

measured on Enceladus and Calypso, the more water ice-rich objects in the Saturn's system Filacchione et al. (2012). Also the 3.1 μm Fresnel peak caused by water ice particles is well-resolved everywhere. Faint features are detected by VIMS at 3.42–3.52 μm resulting compatible with the CH_2 aliphatic stretch signature (see discussion in Section 6).

A synoptic view of the ten VIMS observations analyzed in this work converted in radial spectrograms is given in Fig. 4. These data, correlated with their own observation geometries, are used to infer the spectral indicators discussed in the next sections.

2.3. Evaluation of the errors

With the scope to determine the accuracy of the spectral indicators (spectral slopes, spectral ratios, band depths) discussed in the next sections, we have performed an accurate analysis of the signal-to-noise (SNR) affecting each spectrogram of the dataset. At each wavelength the SNR is defined as the ratio between the raw average signal measured across a 400 km-wide radial bin and the average sky signal, both expressed in digital units. For each mosaic we have used the region outside the F ring to retrieve the sky signal. Both rings and sky observations are taken with the same integration time and operative mode. The resulting error affecting the spectral reflectance measurements is given by $1/\text{SNR}$. With the aim to compare the reflectance and the associated error we report in Fig. 5 the value of the SNR on the rings spectrograms following the same scheme previously used for reflectance in Fig. 4. With the exception of mosaics (VII) and (I), the error is <1% between 0.35 and 2.5 μm: propagating the error we find that spectral slopes/ratios and water ice band depths at 1.5 and 2.0 μm discussed in the next sections are in general affected by errors lower than 1% and 5%, respectively. The scarcity of photon flux causes the increase of the error between 2.5 and 5.1 μm; at 3.6 μm the typical error is in the 15–20% range. Finally, the high phase angle characterizing the two mosaics (VII) (90.4°) and (I) (132.4°) implies much lower SNR conditions across the entire spectral range.

3. Spectral indicators versus distance to Saturn

As shown in Fig. 3, rings reflectances are dominated by water ice across the entire disk. The variability of the numerous and wide-band spectra is well reflected in fewer spectral indicators, which help reducing the complexity of the analysis. In this work we have used the *spectral reflectance $I/F(0.55 \mu\text{m})$* as an indicator correlated to visual albedo and optical depth. The *spectral slope $S_{0.35-0.55}$* is an index of the reddening caused by the presence of chromophores in intraparticle–intramolecular mixing with water ice. The *spectral slope $S_{0.55-0.95}$* is a marker of the reddening caused by the presence of chromophores in areal mixing with water ice. The *water ice 1.5–2.0 μm band depths* are related to the water ice abundance and grain size. Also the $I/F(3.6)/I/F(1.8)$ ratio is a further indicator of regolith grain size. Finally, the *position of the 3.6 μm continuum peak* is a hint of the regolith's grains temperature.

The methods applied to measure spectral slopes and band depths were already discussed in previous papers (Cuzzi et al., 2009; Filacchione et al., 2010, 2012) and are not repeated here for brevity. All these spectral indicators are illumination/viewing geometry, material composition and grain size-dependent. Water ice band depths and $I/F(3.6)/I/F(1.8)$ ratio are temperature-dependent too. Grundy and Schmitt (1998) have measured the changes of the 1.5–2 μm water ice absorptions positions with temperature finding that they move to shorter wavelengths as ice temperature increases. However, given the VIMS spectral resolution, this effect is not optimal to retrieve the typical saturnian ring's temperatures which are between ≈ 40 –120 K, depending on solar elevation angle

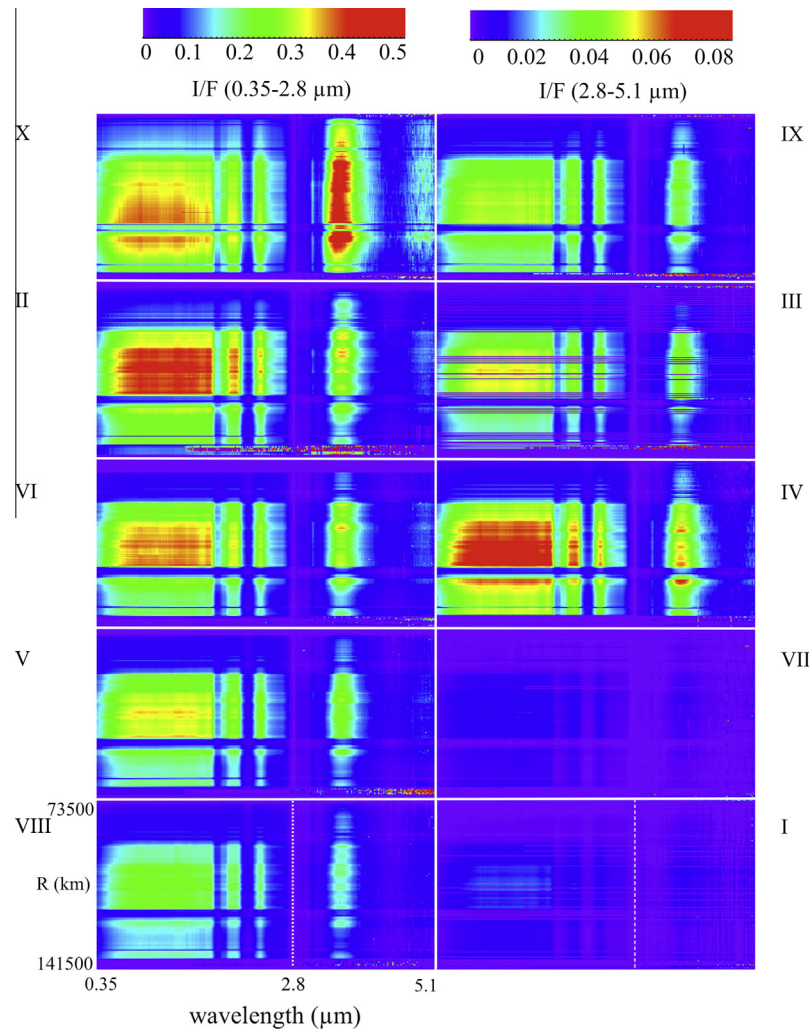


Fig. 4. Reflectance values in rings spectrograms. Left column, from top to bottom: observations (X), (II), (VI), (V), (VIII). Right column, from top to bottom: observations (IX), (III), (IV), (VII), (I). Each spectrogram's image is plotted using two different stretches to improve visualization; the ranges between $0.35\text{--}2.8\,\mu\text{m}$ and $2.8\text{--}5.1\,\mu\text{m}$ are rendered according to the color ramp schemes shown on the top. The legend relative to observation (VIII) (bottom right corner) showing the spectral axis (horizontal) and radial direction (vertical) is valid for each of them. The vertical dot line correspond to the $2.8\,\mu\text{m}$ wavelength where the stretch change occurs. (For interpretation of the references to color in this figure legend, the reader is referred to the web version of this article.)

(season), local time and radial position. As measured by [Grundy and Schmitt \(1998\)](#), in this range of temperatures the $1.5\text{--}2\,\mu\text{m}$ band centers shift of about 4 nm, well below the $16.6\,\text{nm}/\text{band}$ spectral resolution of VIMS-IR. However, laboratory measurements conducted by [Clark et al. \(2012\)](#) have indicated that the position of the continuum peak at $3.6\,\mu\text{m}$ in crystalline water is temperature-dependent and suitable to infer the ring's particle temperature. A specific discussion about the use of the $3.6\,\mu\text{m}$ peak position as a spectral indicator of temperature is addressed in Section 5.

In our discussion about the photometric properties of the ring particles we are following the same assumption made by [Cuzzi and Estrada \(1998\)](#), e.g. that a typical ring particle is a centimeter to meter-sized icy chunk. The spatial distribution, size and shape of these particles drives the local optical depth of the ring. A regolith of icy grains envelops the external skin of the chunks driving the spectro-photometric parameters like the single particle albedo and phase function. Both ring optical depth and spectro-photometric responses of the surface regolith can therefore influence the resulting brightness of the rings.

Since in our analysis we are mainly using observations taken in backscattering geometries and at low ring tilt angles, with the exception of datasets (I) and (X), the effect of the multiple scatter-

ing between chunks can be neglected with respect of the single scattered light, as demonstrated by [Cuzzi et al. \(1984\)](#) using Voyager observations. The photometry study of the A ring by [Dones et al. \(1993\)](#) has demonstrated how single scattered, multiple scattered and Saturn-shine components account for the 0.97, 0.02–0.03 and <0.01 of the rings brightness, respectively, on low phase ($\alpha = 13^\circ$) observations. The same contributions on high phase ($\alpha = 155^\circ$) observations change in 0.03, 0.84 and 0.13, respectively.

The single scattering assumption is not more valid when we study the interaction of photons with regolith's particles: in this case the multiple scattering between grains must be considered, especially to model high phase observations. Furthermore, [Esposito \(1979\)](#) applying Markov chain formalism to radiative transfer has demonstrated that interparticle shadowing plays a minor role in the multiple scattering processes.

3.1. $I/F(0.55\,\mu\text{m})$ radial profiles

The radial profiles of the I/F at $0.55\,\mu\text{m}$ derived from the ten spectrograms are shown in Fig. 6, top panel, at a spatial resolution of $400\,\text{km}/\text{bin}$. The errors associated to the I/F are shown in the same figure, bottom panel. In general the reflectance along the

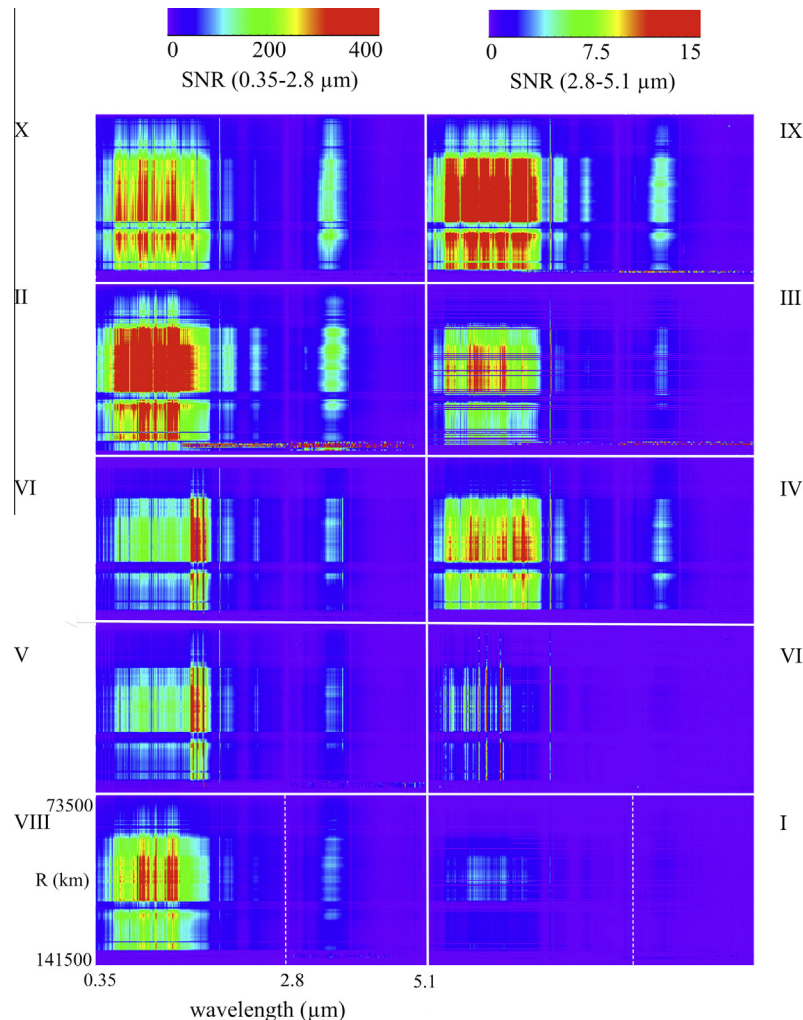


Fig. 5. SNR values in rings spectrograms, visualized with the same scheme used for the reflectance in Fig. 4. Left column, from top to bottom: observations (X), (II), (VI), (V), (VIII). Right column, from top to bottom: observations (IX), (III), (IV), (VII), (I). Each spectrogram's image is plotted using two different stretches to improve visualization: the ranges between 0.35 and 2.7 μm and 2.7 and 5.1 μm are rendered according to the color ramp schemes shown on the top. The legend relative to observation (VIII) (bottom right corner) showing the spectral axis (horizontal) and radial direction (vertical) is valid for each of them. The vertical dot line correspond to the 2.8 μm wavelength where the stretch change occurs. (For interpretation of the references to color in this figure legend, the reader is referred to the web version of this article.)

radial distance follows the trends seen in the spectrograms, with lower values across C ring and CD and higher across A–B rings. The illumination and viewing geometry are responsible of the differences in intensity seen for the same ring region: in general the reflectance decreases when phase angle increases but with some peculiar behavior across different ring regions.

As an example, the A ring reaches the maximum reflectance value, 0.35 at 123,000 km, on low-phase observations (X) (black curve) and (IV) (light green curve). In agreement with the trend seen on Voyager data (Cuzzi et al., 1984), a reverse contrast is observed between the inner and outer part of the A ring: at low phase the reflectance decreases linearly with the radial distance while at intermediate phase ($\approx 20\text{--}30^\circ$) the trend assumes a bowl-shaped profile with two maxima on the inner and outer edges. The outer edge reflectance becomes higher than the inner edge when the phase is high, like on observation (I) (red curve, phase = 132.4°). According to Cuzzi et al. (1984) this effect is caused by the presence of wavelength-sized, or even smaller, e.g. sub-micron scale, forward scattering particles in the outer part of the A ring (for $r > 130,000$ km). However, this explanation is incompatible with high phase transmission spectra which do not exhibit the spectral signatures that one would expect if sub-micron

particles were common (Hedman et al., 2013). Another complexity in comparing A ring observations taken at different illumination and viewing geometry is given by the presence of self-gravity wakes which cause azimuthal asymmetry in brightness (Thompson et al., 1981; Dones et al., 1993) and in optical depth along the line of sight (Colwell et al., 2006; Hedman et al., 2007).

Similarly, B ring radial features exhibit stronger contrast on all observations taken at phase larger than $20\text{--}30^\circ$. On low phase observations, like on (X) (black curve, phase = 5.7°) the reflectance linearly decreases with the radial distance moving from outer to inner B ring resulting in a low contrast profile. The step-like transition zone located at $r \approx 98,000$ km between B1–B2 seen on high phase observations becomes smoother at low phase, e.g. on (X).

3.2. Spectral slopes $S_{0.35\text{--}0.55}$ and $S_{0.55\text{--}0.95}$ radial profiles

As discussed in Cuzzi et al. (2009) and in Filacchione et al. (2012) spectral slopes $S_{0.35\text{--}0.55}$ and $S_{0.55\text{--}0.95}$ are markers for the presence of contaminants/darkening agents bound with the water ice regolith covering the ring particles.

The spectral slope $S_{0.35\text{--}0.55}$ profile, shown in Fig. 7, gives us clues about the reddening caused by the presence of chromophores

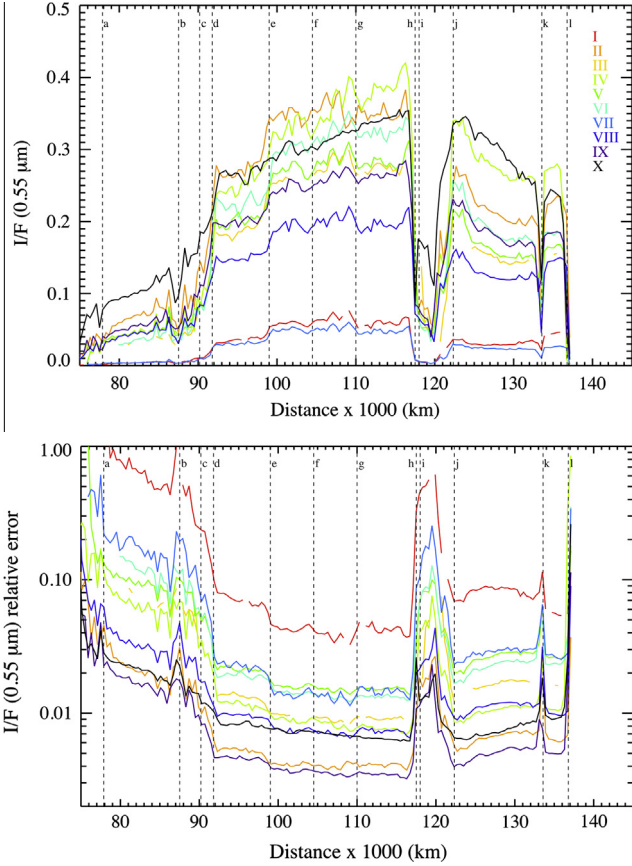


Fig. 6. I/F($0.55\text{ }\mu\text{m}$) radial profiles (top panel) and errors (bottom panel). Observations labels follow the nomenclature given in Table 1. Vertical dash lines indicate the position of the following relevant ring structures: (a) Titan ringlet, (b) $1.47 R_{\text{S}}$ ringlet, (c) $1.495 R_{\text{S}}$ ringlet, (d) C-B ring boundary, (e) B1–B2 boundary, (f) B2–B3 boundary, (g) B3–B4 boundary, (h) B4–CD boundary, (i) Huygens gap, (j) CD–A ring boundary, (k) Encke gap, (l) A ring outer edge. The B ring regions are coded following the nomenclature given in Marouf et al. (2006).

in intraparticle–intramolecular mixing with water ice. As a general rule when the slope increases the reflectance spectrum becomes more red as a consequence of higher amount of contaminants. As a reference, pure water ice has a null slope being neutral or colorless in the 0.35 – $0.55\text{ }\mu\text{m}$ spectral range. For a given phase, VIMS measures maximum values of the $S_{0.35}$ – 0.55 across the A (outer region) and B rings; the slope decreases from the middle of the A ring towards the outer edge of CD. A similar effect is caused by an increase of contaminants with respect to the outer regions of the A ring.

Moving to the B ring we observe that $S_{0.35}$ – 0.55 slope is characterized by small relative variations showing a local maximum around $r = 100,000\text{ km}$ and a minimum around $r = 102,000\text{ km}$; the peak placed at $r = 100,000\text{ km}$ may identify a region with purer ices because the maximum in the $S_{0.35}$ – 0.55 slope is correlated with a similar peak in the water ice band depth. As discussed in Nicholson et al. (2008), the $S_{0.35}$ – 0.55 profile is closely correlated with the water ice band depth profiles (discussed later and shown in Figs. 9 and 10). In the outer part of the B ring the slope seems to decrease with the radial distance showing small contrast across the ring in the low and intermediate phase observations. On the high phase data, like observations (I) (red curve, phase = 132.4°) and (VII) (light blue curve, phase = 96°) the trend is more flat and locally-variable.

The $S_{0.35}$ – 0.55 slope profiles have minima across C ring and CD where the intraparticle–intramolecular mixing of contaminants

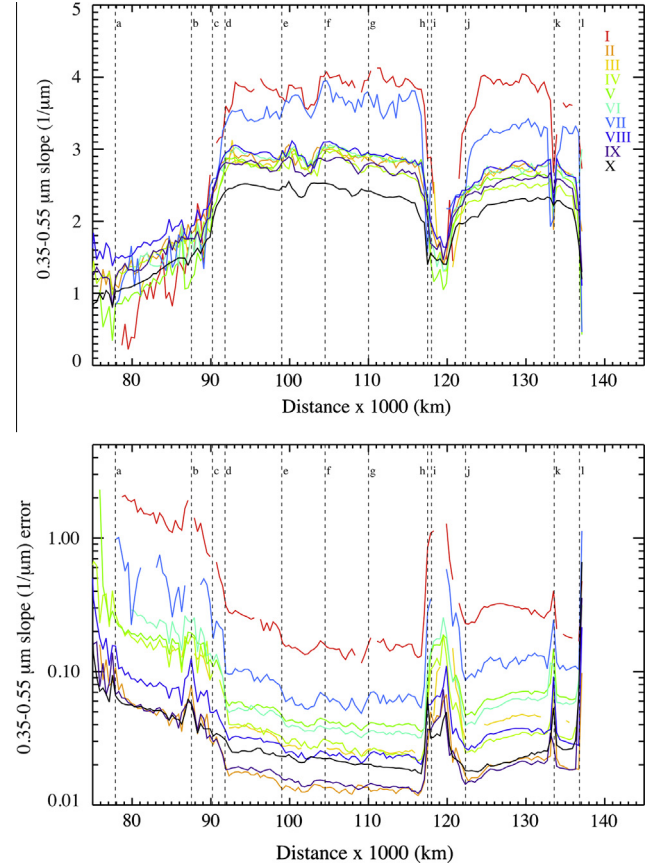


Fig. 7. Spectral slope $S_{0.35}$ – 0.55 radial profiles (top panel) and errors (bottom panel). At high phases a significant increase in slope (reddening) is observed. Labels follow the same scheme described in Fig. 6.

within water ice is minimal. In these regions where small grain size particles prevail, the optical depth and the surface mass density are smaller with respect to A and B rings. Note that the low signal to noise affecting high phase observations (I and VII) causes fluctuations in the slope values measured across these two regions. VIMS data show a regular trend in the distribution of the $S_{0.35}$ – 0.55 slope which increases with the phase angle: across A and B ring it moves, in average, from a value of $3\text{ }\mu\text{m}^{-1}$ at phase 5.7° (X, black curve) to more than $4\text{ }\mu\text{m}^{-1}$ at phase 132.4° (I, red curve). Such values are the higher observed across rings and satellites' surfaces of the Saturn's system Filacchione et al. (2012): as reported by Estrada and Cuzzi (1996) A and B rings are very “red” objects, especially at high phases.

The spectral slope $S_{0.55}$ – 0.95 profile (Fig. 7) is an indicator of the presence of chromophores in areal or intimate mixing with water ice particles. Pure water ice has a neutral to moderately negative (or blue) slope in this spectral range. In general the $S_{0.55}$ – 0.95 slope is characterized by a flat profile across A and B rings, with values of about 0 – $0.1\text{ }\mu\text{m}^{-1}$ on low phase observation (X) (black curve); this is in agreement with a water ice-rich spectral behavior. VIMS observations evidence the slope's increase across CD and C ring resulting in the opposite behavior with respect to what we have seen for the $S_{0.35}$ – 0.55 slope. Across these low optical depth regions the $S_{0.55}$ – 0.95 slope becomes more intense as a result of the presence of a larger fraction of dark material particles dispersed among ice grains. This is in agreement with the Cuzzi and Estrada (1998) ballistic transport model in which is foreseen a similar accumulation of residual dark material of meteoritic and cometary origin in the C ring and CD.

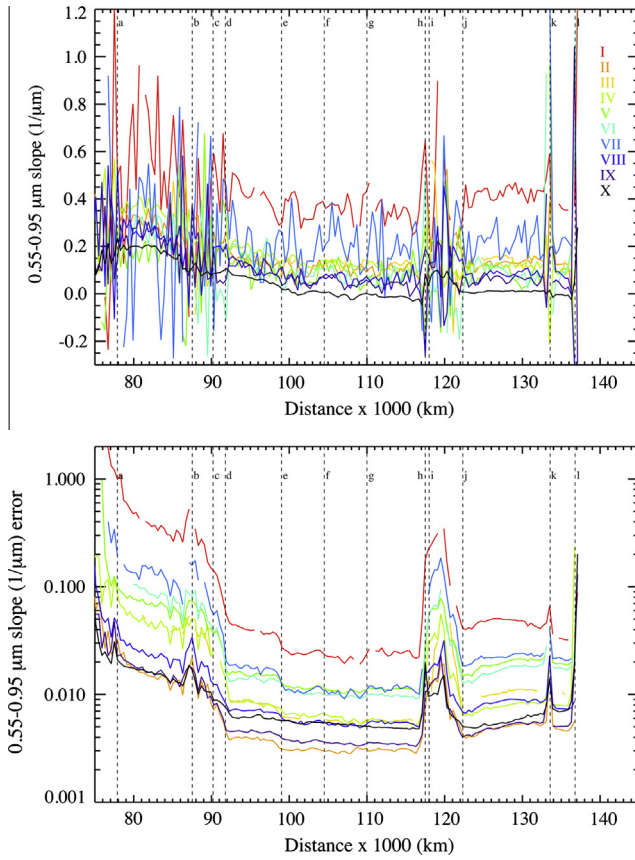


Fig. 8. Spectral slope $S_{0.55-0.95}$ radial profiles (top panel) and errors (bottom panel). At high phases a significant increase in slope (reddening) is observed. Labels follow the same scheme described in Fig. 6.

Similarly with the $S_{0.35-0.55}$ slope, also the $S_{0.55-0.95}$ slope shows a phase angle-dependence across A and B rings, increasing from $\approx 0-0.1 \mu\text{m}^{-1}$ at phase 5.7° (observation X, black curve) to about $0.4 \mu\text{m}^{-1}$ at phase 132.4° (observation I, red curve).

3.3. Water ice 1.5–2.0 μm band depth radial profiles

The two water ice 1.5–2.0 μm band depths are spectral indicators suitable to determine the water ice abundance and the grain size. The profiles retrieved from VIMS spectrograms show similar trends across rings (see Figs. 9 and 10): the water ice band depth is minimum across C ring and CD while maximum is reached across A and B rings. Starting from low phase observation (X), black curve, phase = 5.7° , the 1.5–2.0 μm band depths have values of about 0.2–0.45 on the inner part of the C ring to about 0.47–0.68 on the outer, respectively. Between the $1.495 R_S$ ringlet and the C–B ring boundary the water ice band depth follows a step ramp. Across the B ring is possible to recognize the inner part, B1–B2, and the outer region, B3–B4: across B1 region the 1.5 μm band depth is about 0.5 (0.7 for the 2.0 μm band) while in B3–B4 both band depths increase about 0.05 reaching 0.55 and 0.75, respectively. In the central B2 ring (from 98,500 to 104,000 km), we observe a peak of higher band depth which can be explained by the presence of more pure, resurfaced water ice correlated with higher optical depth occurring in this region. The minimum value of the 1.5 μm band depth on the middle of the CD is about 0.4; for the 2.0 μm band depth is 0.62. From here the band depths follow a “parabolic” trend increasing from CD to reach the maximum on the outer part of the A ring in a way very similar to the $S_{0.35-0.55}$ profile previously shown in Fig. 7. A similar effect can be explained

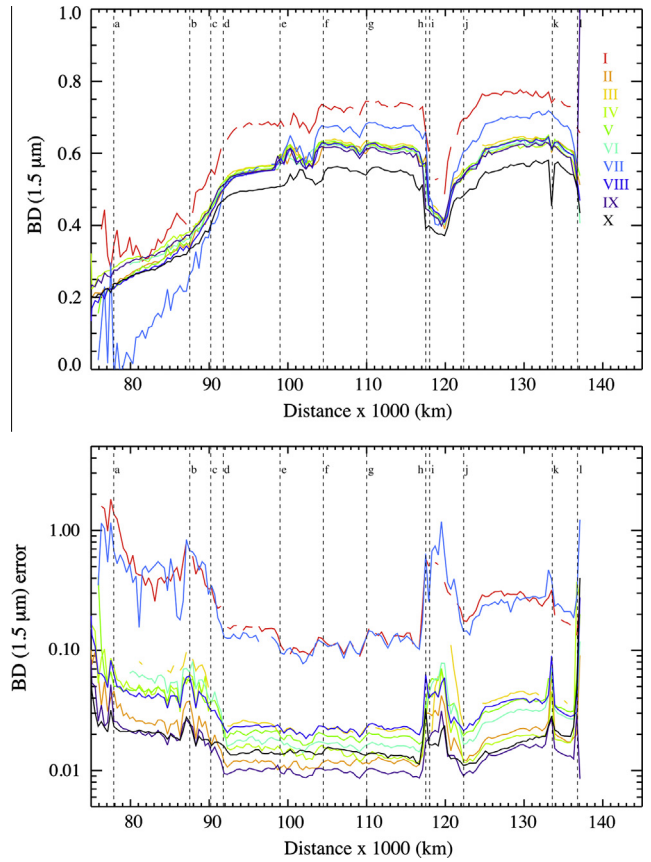


Fig. 9. Water ice 1.5 μm band depth radial profiles (top panel) and errors (bottom panel). Labels follow the same scheme described in Fig. 6.

by supposing a progressive increase of non icy material bound in water ice grains at molecular scale Nicholson et al. (2008): the advantage of this kind of mixing is to not influence the $S_{0.55-0.95}$ profile, which remains constant, because this spectral range is more sensitive to detect the fractional abundance changes of the non icy material, nor to change the $I/F(0.55 \mu\text{m})$ profile, which is dependent on optical depth. The maximum values of the band depths on the A ring are in general larger than the similar one measured on the B ring: 0.68 and 0.76 for the 1.5–2.0 μm band depth, respectively.

On both profiles shown in Figs. 9 and 10 we observe a noteworthy increase of the band depth values with the phase angle. On observation (I), red curve, phase = 132.4° , the A ring maximum values of the 1.5–2.0 μm band depths are about 0.78–0.87, respectively: this means an increment of about 0.1 with respect to low phase observations. The band depth changes with phase as a consequence of the balance between single scattering and forward-multiple scattering processes. At high phases the forward-multiple scattering component within the regolith dominates across the entire absorption band (Hapke, 1993) causing an increment of the band depth. Conversely, the band depth decreases at low phases because in this case the multiple scattering is predominant on the band wings where the single scattering albedo, w , is higher. At the same time the multiple scattering is less effective at the band center where w is low allowing the single scattering to prevail (Veverka et al., 1978; Hapke, 1993). As a consequence of this effect the band depth decreases. We have observed that water ice band depths are almost constant for phases in the 20 – 30° interval: in this range in fact the single scattering dominates throughout the entire absorption band.

Finally, we report about the typical dimension of the regolith grain sizes covering the surface of the ring particles. Assuming a

pure water ice composition and selecting observations taken at phases of about 30° is possible to apply the method described in Clark and Lucey (1984) which allow us to correlate the band depth with the grain size. In Fig. 10 three arrows along the vertical axis are placed in correspondence of the $2.0\text{ }\mu\text{m}$ band depth values for 10, 40 and 100 μm grain sizes. Comparing these values with the profile of observations (II), orange curve, phase = 30.7° or (IV), lime green curve, phase = 29.2° , is possible to infer typical regolith grain sizes between $20\text{--}50\text{ }\mu\text{m}$ in the C ring, $50\text{--}60\text{ }\mu\text{m}$ in the CD and $\approx 80\text{--}100\text{ }\mu\text{m}$ in the A and B rings. Of course the presence of contaminants, clearly evidenced by the visible $S_{0.55\text{--}0.95}$ spectral slope, influences the estimation of the grain size on C ring and CD with this method. For a given grain size when a darkening material is mixed with water ice both the 1.5 and $2.0\text{ }\mu\text{m}$ band depths decrease (see as example Fig. 5 in Filacchione et al., 2010). As a result, the grain size derived with this method assuming pure water ice composition could be underestimated.

3.4. $I/F(3.6) / I/F(1.8)$ ratio radial profile

The $I/F(3.6) / I/F(1.8)$ ratio is another appropriate indicator to infer the regolith grain size in case of pure water ice composition. In a previous paper (Filacchione et al., 2012) we have analyzed the effect of the regolith grain size on the continuum levels at 1.8 and $3.6\text{ }\mu\text{m}$: for pure water ice these two continuum levels are strongly grain size-dependent, reaching high values for small grains (few microns) and low values for large particles (hundred microns). After having calibrated the ratio with laboratory and synthetic spectra we have seen that it decreases from 0.406 to 0.164 to

0.096 for $10, 50$ and $100\text{ }\mu\text{m}$ grain sizes, respectively. These values, like for the similar grain size retrieval from the $2\text{ }\mu\text{m}$ band depth we have discussed in the previous section, is valid only for observations taken at phases of about 30° like (II), orange curve, phase = 30.7° or (IV), lime green curve, phase = 29.2° reported in Fig. 11. VIMS data point out that the ratio profiles have a large variability along the radial distance showing two peaks across the C ring and CD while minimum values are measured on the A and B rings. This general radial trend remains for the different observations independently from the phase angle. However, the ratio values show a net decrease when phase increases: in the middle of the A ring the $I/F(3.6) / I/F(1.8)$ ratio drops from about 0.2 to 0.08 between observations (X), black curve, phase = 5.7° and (I), red curve, phase = 132.4° . This is a consequence of the multiple scattering which dominates over single scattering at high phases reducing more the reflectance at $3.6\text{ }\mu\text{m}$ than at $1.8\text{ }\mu\text{m}$. The five arrows along the vertical axis in Fig. 11 indicate the reference values of the $I/F(3.6) / I/F(1.8)$ ratio for grain sizes between 10 and $100\text{ }\mu\text{m}$: comparing them with the 30° phase observations, e.g. (II), (III), (IV) and (V), we measure a typical regolith grain size of about $20\text{--}50\text{ }\mu\text{m}$ in C ring, $<30\text{ }\mu\text{m}$ in the CD and $50\text{--}80\text{ }\mu\text{m}$ in A-B rings.

In conclusion, the regolith grain sizes derived by applying two different spectral indicators, i.e. the $2.0\text{ }\mu\text{m}$ band depth and $I/F(3.6) / I/F(1.8)$ ratio, converge on very similar results. At the same time the general trend observed across the rings, with smaller grains in the C ring and in the CD and larger one in the A and B rings, is confirmed by both methods.

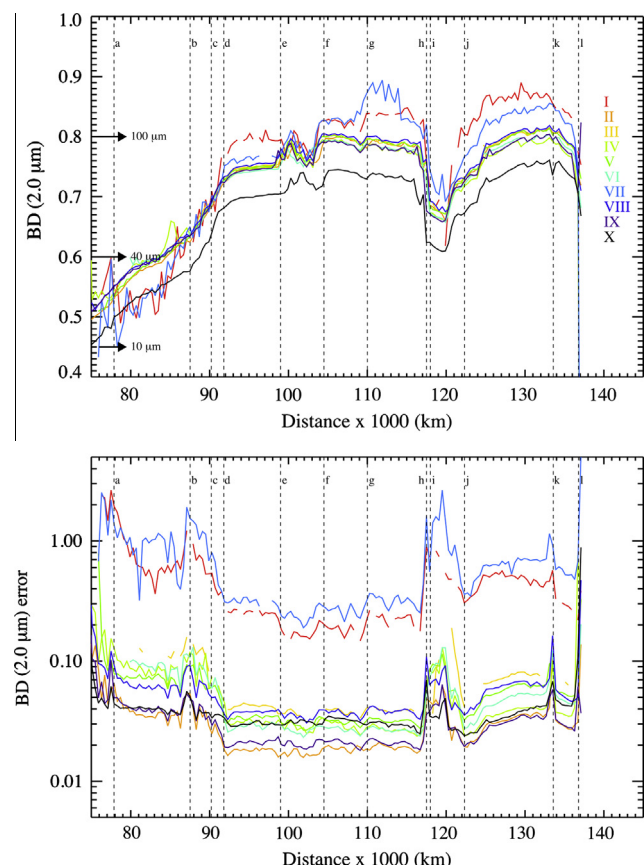


Fig. 10. Water ice $2.0\text{ }\mu\text{m}$ band depth radial profiles (top panel) and errors (bottom panel). Reference band depth values for pure water ice grains of different diameters (from 10 to $100\text{ }\mu\text{m}$) are indicated. Labels follow the same scheme described in Fig. 6.

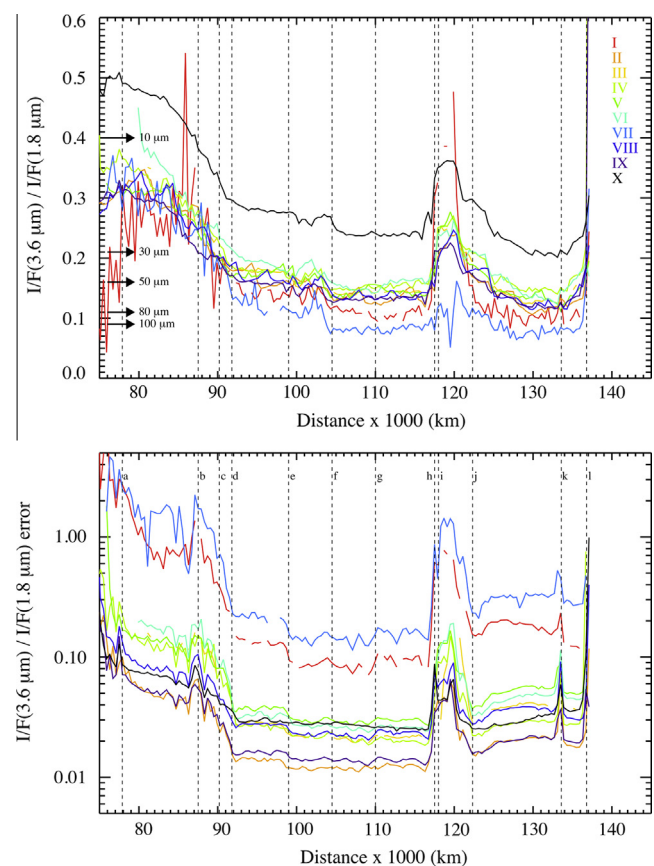


Fig. 11. $I/F(3.6) / I/F(1.8)$ ratio radial profiles (top panel) and errors (bottom panel). Reference values for pure water ice grains of different diameters (from 10 to $100\text{ }\mu\text{m}$) are indicated. Labels follow the same scheme described in Fig. 6.

4. Spectral indicators: phase-dependent effects

As described in the previous section, spectrograms are an effective tool to build radial profiles across rings which, through the use of many observations taken at different illumination and viewing geometries, allow us to disentangle spectral properties from photometric effects: a similar approach is essential to understand the physical properties of the ring particles and to study the interaction of the solar radiation with them. For these reasons we focus this section to investigate the relations observed between spectral indicators and phase angle.

The scatterplot in Fig. 12 shows the dispersion of the visible spectral slopes $S_{0.35-0.55}$ – $S_{0.55-0.95}$ for the main four ring regions (A, B, C ring and CD) as observed on five observations taken with the phase angle running between 5.7° and 132.4°. A similar study for both spectral slopes and band depths applied to a large dataset of Saturn's icy satellites and one ring mosaic is already published in (Filacchione et al., 2012). At low phase (5.7°, black symbols) A-B ring points (indicated as squares and diamonds, respectively) are characterized by maximum $S_{0.35-0.55}$ slope values, between 2.5–3 μm^{-1} and almost neutral $S_{0.55-0.95}$, between 0 and 0.1 μm^{-1} . C ring (circles) slopes have minimum $S_{0.35-0.55}$ slope values, clustered around 1.4 μm^{-1} while the $S_{0.55-0.95}$ slope is about 0.2 μm^{-1} . Between these two clusters the CD points (triangles) are grouped around values of 2.0 μm^{-1} and 0.05 μm^{-1} for the $S_{0.35-0.55}$ and $S_{0.55-0.95}$ slope, respectively.

This trend means that Saturn's ring are characterized by a different spectral response in the two visible ranges 0.35–0.55 μm and 0.55–0.95 μm . As is possible to observe also in Figs. 2 and 3, a very steep (red) slope below 0.55 μm and a relatively flat continuum between 0.55 and 0.95 μm characterizes both A and B rings reflectance spectra. In general B ring points are a few percent more red than the A ring ones in the $S_{0.35-0.55}$ slope; C ring and CD spectra appear less red than A-B rings in the 0.35–0.55 μm range but more red between 0.55 and 0.95 μm .

When phase increases this general distribution of the slopes values does not change in relative terms but the four clusters move towards higher values. At 132.4° (red symbols) the clusters appear

more dispersed than in the low observation case as a consequence of the lower SNR conditions (Fig. 5). For the A-B ring points at 132.4° phase angle we measure an increment of about 1 and 0.4 μm^{-1} for the $S_{0.35-0.55}$ and $S_{0.55-0.95}$ slope, respectively, with respect to the low phase observation. Similarly, for the C ring and the CD the increment is of about 0.8 and 0.4 μm^{-1} for the two slopes.

The analysis of the water ice 1.5 and 2.0 μm band depths taken at different phase angles is summarized in Fig. 13. The ring points are aligned along a branch, showing an almost linear distribution with both band depths increasing from the C ring and the CD up to the A and B rings. On low phase (5.7°, black symbols) observation the minimum band depths are measured across the C ring (circles) where $BD(1.5 \mu\text{m}) = 0.2-0.5$, $BD(2.0 \mu\text{m}) = 0.45-0.7$. The CD points (triangles) are grouped in the $BD(1.5 \mu\text{m}) = 0.35-0.5$, $BD(2.0 \mu\text{m}) = 0.6-0.68$ ranges. Finally, the A and B rings (squares and diamonds respectively) define the upper edge of the distribution, with maxima placed approximately at $BD(1.5 \mu\text{m}) = 0.64$, $BD(2.0 \mu\text{m}) = 0.82$ and minima at $BD(1.5 \mu\text{m}) = 0.45$, $BD(2.0 \mu\text{m}) = 0.68$. Observations taken at 19.2° (blue symbols) and 30.7° (cyan symbols) phases show very similar trends but shifted to few percent higher band depths with respect to the 5.7° phase branch.

The distribution changes when phase reaches 96°: here the $BD(1.5 \mu\text{m})$ shows a large variability, between 0 and 0.4 across the C ring (circles) and deviates with respect to the trend shown at lower phases. Another significant change is observed on the top edge of the distribution where A and B ring points are clearly separated between them. B ring points (diamonds) are divided in two subgroups, the first around $BD(1.5 \mu\text{m}) = 0.55$, $BD(2.0 \mu\text{m}) = 0.76$ which corresponds to B1 region ($r < 100,000 \text{ km}$); the second around $BD(1.5 \mu\text{m}) = 0.67$, $BD(2.0 \mu\text{m}) = 0.88$ includes the points in the B2-B4 regions ($r > 100,000 \text{ km}$). At this phase the A ring points (squares) are all grouped in a single cluster between $BD(1.5 \mu\text{m}) = 0.6-0.75$, $BD(2.0 \mu\text{m}) = 0.76-0.86$. Finally, at 132.4° phase (red symbols) across the A ring (squares) the maximum value of the two band depths is reached, 0.78 and 0.89, respectively for $BD(1.5 \mu\text{m})$ and $BD(2.0 \mu\text{m})$. At this high phase the entire branch is shifted towards higher values of the $BD(1.5 \mu\text{m})$.

This scatterplot shows the relationship between the spectral slopes $S_{0.35-0.55}$ (x-axis, ranging from 0 to 5 μm^{-1}) and $S_{0.55-0.95}$ (y-axis, ranging from 0.0 to 1.0 μm^{-1}). The plot is divided into four main regions representing different ring regions: C ring (circles), B ring (diamonds), CD (triangles), and A ring (squares). Data points are color-coded according to their phase angle: 5.7° (black), 19.2° (blue), 30.7° (cyan), 96.0° (green), and 132.4° (red). The C ring points are clustered at lower slopes, while the A ring points are at higher slopes. The CD points are intermediate. The phase angle color bar is located in the bottom right corner of the plot area.

Fig. 12. Scatterplot of the spectral slope $S_{0.35-0.55}$ versus $S_{0.55-0.95}$ for rings observations taken at 5.7°, 19.2°, 30.7°, 96.0° and 132.4° phase angles.

This scatterplot shows the relationship between the water ice band depths $BD(1.5 \mu\text{m})$ (x-axis, ranging from 0.0 to 0.8) and $BD(2.0 \mu\text{m})$ (y-axis, ranging from 0.4 to 1.0). The plot follows a similar structure to Fig. 12, with four main ring regions: C ring (circles), B ring (diamonds), CD (triangles), and A ring (squares). Data points are color-coded by phase angle: 5.7° (black), 19.2° (blue), 30.7° (cyan), 96.0° (green), and 132.4° (red). The points form a distinct linear trend from the C ring at the bottom left to the A ring at the top right. The phase angle color bar is located in the bottom right corner of the plot area.

Fig. 13. Scatterplot of the water ice band depths at 1.5 and 2.0 μm for rings observations taken at 5.7°, 19.2°, 30.7°, 96.0° and 132.4° phase angles.

VIMS data reveal that both VIS slope $S_{0.35-0.55}$ (Fig. 14) and 2.0 μm water ice band depth (Fig. 15) are phase-dependent and that a similar behavior is common for both dense A and B rings and optically thin CD and C ring regions. The band depth is almost constant in a small phase interval between $\approx 20^\circ$ and 40° angles in which the single scattering dominates throughout the entire band width.

In order to understand how the spectral parameters are influenced by illumination conditions, the interaction of light with the ring particles must be considered. In the limit of the single scattering theory (Dones et al., 1993), the reflection function of the rings, assumed as a many-particles thick layer, is given by:

$$R(\mu, \mu_0, \alpha) = \frac{w}{4(\mu + \mu_0)} P(\alpha) \left(1 - e^{-\tau \frac{\mu_0 + \mu}{\mu \mu_0}}\right) \quad (1)$$

where $\mu = |\sin(B)|$ with B the observer's elevation angle, $\mu_0 = |\sin(B')|$ with B' the solar elevation angle, w is the single scattering albedo of a ring particle and $P(\alpha)$ is the particle's disk-integrated phase function which describes the angular distribution of the scattered radiation at phase angle α and τ is the extinction optical depth. Using this law is therefore possible to infer the reflectance of a given region of the rings assuming to know the optical depth τ , the single scattering albedo w and the particle's phase function $P(\alpha)$. Among these three parameters the phase function plays a fundamental role because several different functions can be used to model the angular response of the radiation scattered by particles: in general large particles – where for large we mean larger than the wavelength of light – have a backscattering response while small dust grains are more forward scattering and isotropic. While the phase function can be modeled and inferred from observations, it remains wavelength-independent, e.g. in the single scattering approximation (Eq. (1)) the reflectance changes by the same quantity across the entire spectral range when phase changes. This means that additional effects must be considered, like the multiple and the intraparticle scattering, in order to match the increase of spectral slopes (Fig. 14) and band depth (Fig. 15) values at high phases observed by VIMS. As verified by Dones et al. (1993) on Voyager data, single scattering approximation gives satisfactory results only on low phase observations while at high phase the multiple scattering becomes predominant on single scattering.

In order to include the effects of multiple and intraparticle scattering among the ring particles we have developed a Monte Carlo model adapted to simulate photons scattering in particulate media of a given composition (Ciarniello et al., 2014). A future paper (II), currently in preparation, shall address these arguments.

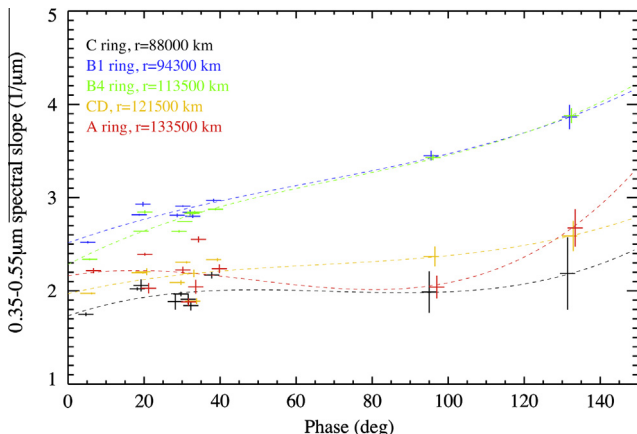


Fig. 14. Spectral slope $S_{0.35-0.55}$ phase curves for average ring regions.

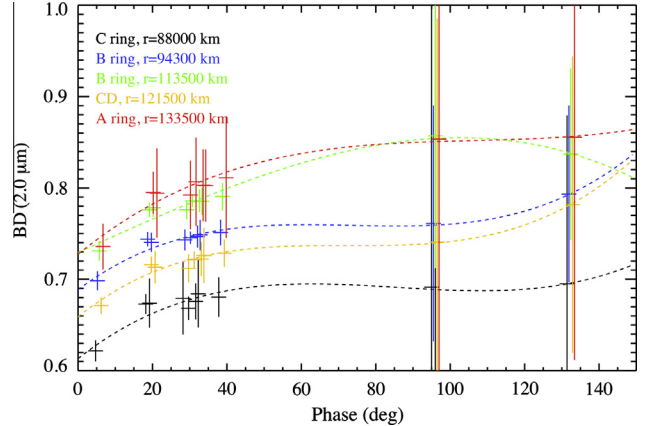


Fig. 15. Water ice 2.0 μm band depth phase curves for average ring regions.

5. Spectral indicators: the temperature-dependent 3.6 μm continuum peak position

As discussed in Section 3, the position of the 3.6 μm continuum peak of crystalline water ice is temperature-dependent and can be inferred using laboratory data. This effect is particularly evident on the imaginary part of the refractive index of crystalline water ice as measured by Mastrapa et al. (2009) for a range of temperature between 20 and 150 K. Rather than using optical constants we have preferred for our analysis to use measurements in reflectance realized by Clark et al. (2012) on small grains of pure water ice at standard illumination conditions (phase = 30°) for temperature of the sample varying between 88 K and 172 K. The lack of laboratory reflectance data at temperature below 88 K do not allow us to measure temperatures below this limit. A simple extrapolation of the trend at lower temperature seems risky because the shift is not linear with temperature. It is well known that ring particles can reach temperatures as low as 50 K at equinox; however, we are measuring the position of the 3.6 μm continuum peak for all observations, leaving the possibility to infer lower temperatures when new laboratory data shall be available. The analysis of the reflectance spectra derived from Clark et al. (2012) measurements (Fig. 16) evidences that the 3.6 μm peak shifts towards shorter wavelengths when the ice is cooled, moving from about 3.675 μm at $T = 172$ K to about 3.581 μm at $T = 88$ K. Starting from this experimental evidence we have used a 4th-degree polynomial fit between 3.2 and 3.8 μm to measure the wavelength at which the peak occurs on laboratory data with the view toward using it as a marker to retrieve the temperatures of the ring particles on the ten spectrograms considered in this work (Table 1). The results of the fit on laboratory data are reported in Fig. 16 for seven measurements taken at temperature between 88 K and 172 K.

The same fitting technique is applied to each one of the 170 average spectra forming a VIMS observation spectrogram. The 3.6 μm peak's profiles as function of the radial distance at 400 km/bin spatial resolution are shown in Fig. 17, left panel. VIMS data highlight some peculiar trends on these observations: (a) in general peak's position, e.g. temperature, and the optical depth are anticorrelated: low optical depth C ring and CD have higher temperatures than A-B rings where the optical depth is higher; (b) with the exception of the CD, the peak's position, e.g. temperature, decreases with distance from Saturn; (c) since the observations shown in Fig. 17 are sorted according to the date of acquisition which increases from year 2004 to 2010, is possible to follow the seasonal changes in peak's position, e.g. temperature. During this period of time the solar elevation angle decreases, becomes null at equinox and finally rises again in 2010. Before

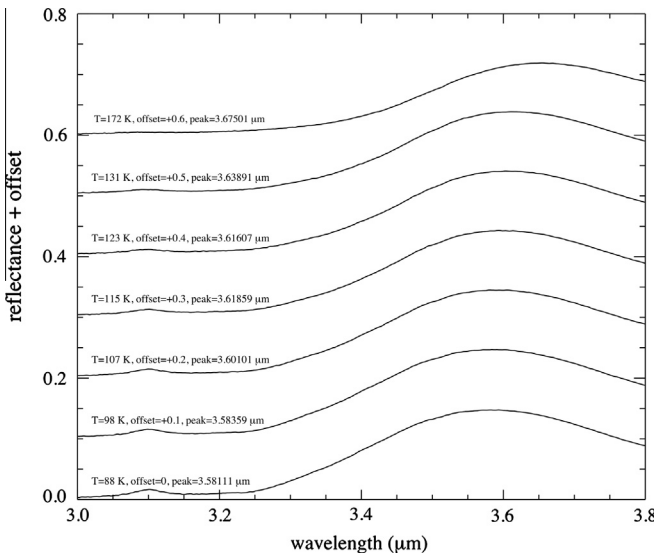


Fig. 16. Water ice reflectance spectra between 3.0 and 3.8 μm showing the shift of the 3.6 μm peak position induced by the temperature. The peak position, evaluated through a 4th-degree polynomial fit between 3.2 and 3.8 μm , moves from 3.67 to 3.58 μm when temperature decreases from 172 to 88 K.

equinox the south side of the ring plane is illuminated while after equinox the sun shines on the north face. Particles are cooling down from summer to equinox. At equinox the solar rays are parallel to the ring plane: as a consequence the particles reach minimum temperature and the peak's position shifts at shorter wavelengths; (d) when both solar and antisolar ansae observations are available, like in (V)–(VI) and (VIII)–(IX), it is possible to distinguish diurnal variations: in those cases across the solar ansa, (V)–(VIII), are measured higher temperatures than on the antisolar, (VI)–(IX). This effect is particularly evident on the C ring.

5.1. Comparison between VIMS and CIRS temperature radial profiles

In order to assess VIMS temperature results we have compared them with simultaneous measurements performed by Cassini CIRS experiment (Kunde, 1996). CIRS ring scans were acquired by the FP1 channel, an infrared interferometer covering the spectral range between 600 and 10 cm^{-1} (17 μm –1 mm) with a 4 mrad circular FOV (Flasar et al., 2004). Temperature of the ring particles by CIRS is derived by applying the same method described in Spilker et al. (2006) and Altobelli et al. (2008). With the exclusion of observations (IV)–(V)–(IX), for all the other seven VIMS observations corresponding CIRS data taken at the same time are available. Compared with VIMS mosaics, CIRS scans shown in Fig. 17, right panel, were acquired with much different spatial samplings: only on observations (II)–(VIII)–(X) are available data spanning continuously across inner C to outer A ring with a regular radial sampling every \approx 60–100 km. For the remaining cases the spatial sampling is much more sparse. The temperature spread observed at some radial distances on some scans (like at $r = 75,000$, 82,000, 106,000 and 109,000 km on observation (I)) corresponds to CIRS long-time measurements at a fixed radial distance planned with the scope to measure the azimuthal temperature's variation of the rings. On this dataset in average the temperature measured by CIRS is affected by an absolute error ≤ 2 K on A–B rings and ≤ 4 K on C ring and CD.

The comparison of VIMS and CIRS observations reported in Fig. 17 reveals that they have the same radial temperature trends. In particular we have found a substantial agreement between VIMS and CIRS results across A and B rings while VIMS measures higher

temperatures than CIRS across C ring and CD. To better understand these differences we focus our analysis on observation (II) for which well-resolved datasets for both instruments are available. On VIMS observation (II) (Fig. 17, left panel, orange curve), having a phase of 30.7° and a solar elevation angle of -22° , the 3.6 μm peak position decreases from about 3.65 μm or $T \approx 148$ K on the inner C ring to about 3.615 μm or $T \approx 115$ K on the outer C ring. Similar values are retrieved through the inner B1 ring. The peak moves to 3.595 μm or $T \approx 105$ K in the B2–B3 regions to reach a minimum 3.58 μm or $T \approx 88$ K on the outer B4 region. On the CD VIMS measures a local peak at 3.615 μm or $T \approx 115$ K while 3.595 μm or $T \approx 105$ K is reached in the inner A ring and 3.58 μm or $T \approx 88$ K on the outer A ring. On the corresponding CIRS observation II (Fig. 17, right panel, orange points) temperature decreases from about 107 K on the inner C ring to about 90 K on the border between C–B rings ($r = 92,000$ km). This means that VIMS measures a temperature higher by 40 K on the inner C ring and about 25 K on the outer. Moving across the B2 ring, CIRS detects a double peak structure at $r = 100,000$ – $105,000$ km where the temperature rises up to 94 K. On the outer B4 ring ($r = 117,000$ km) CIRS temperature decreases to ≈ 89 K. Therefore on the B ring VIMS temperature is only few K higher than CIRS. The maximum temperature CIRS has measured on the CD is 100 K while VIMS records ≈ 115 K, 15 K more than CIRS. Finally, on the A ring CIRS measures an almost linear decrease of the temperature from about 90 K on the inner boundary to ≈ 82 K on the outer. Similarly, VIMS temperature profile decreases from ≈ 105 K to 88 K.

From this comparison is evident that C ring and CD temperatures measured by VIMS through the 3.6 μm peak position method are in general much higher than corresponding ones reported by CIRS. There are multiple possible explanations for this discrepancy that need to be explored, including the deviation of the peak's position in presence of contaminants, in particular organics (see Section 6) which having absorption bands falling in the 3.6 μm peaks short-wavelength wing may change the apparent position of the peak: as a consequence of the erosion of the continuum at shorter wavelengths the peak position appears at longer wavelengths, e.g. at higher equivalent temperature; in the ring's particles distribution properties (grain size, surface roughness, ring's optical depth); or in the illumination geometry – especially at very high and low illumination angles. Another important effect to consider is the different skindepth sampled by the two instruments as a consequence of the very different wavelengths at which they operate: while VIMS is sensitive to a very shallow skindepth (few microns) from the outer surface of the particles, CIRS measures temperature at greater depth (few millimeters). Therefore VIMS performs a “surface” temperature measurement while CIRS integrate in a “volume”.

As mentioned at the beginning of this section VIMS and CIRS datasets allow us to follow how seasonal changes induced by the variation of the solar elevation angle affect the ring temperature. In the time interval considered in this work, the solar elevation angle decreases from -23.5° in 2004 to 0° in 2009 (equinox) to increase to 2.6° in 2010. The south face of the ring plane is observed by VIMS in reflectance when the sub-solar latitude is negative (observations I to IX) while when is positive (X) the north face is seen. Furthermore, when the solar elevation angle approaches 0° (equinox) the ring plane is no more directly illuminated by the Sun but it receives only the saturnshine and Saturn's thermal flux on dayside part of the orbit while only the Saturn's thermal emission at $T = 95$ K is radiated on the nightside. In this geometry, in absence of the direct solar flux, the particles cool down: according to Spilker et al. (2013) the ring temperatures measured by CIRS at equinox were 55–75 K for the C ring, 45–60 K for the B ring, 45–58 K for the CD and 43–52 K for the A ring.

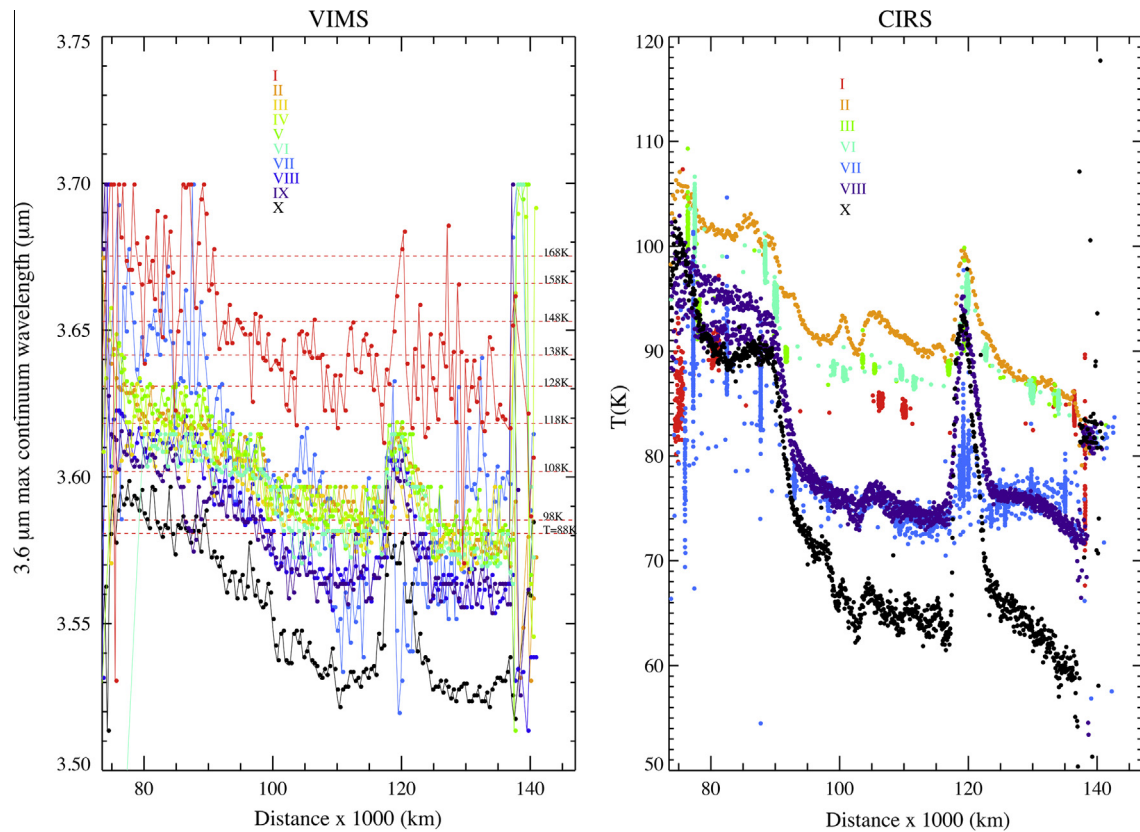


Fig. 17. Left panel: VIMS-retrieved 3.6 μm maximum continuum wavelength and corresponding water ice temperature scale (horizontal dashed lines) for the 10 observations considered in this work. From observation (I) to (X) the sub-solar latitude, or solar elevation angle, decreases from -23.5° to 2.6° . When the sub-solar latitude is negative VIMS observes the south face of the ring plane, (I) to (IX), when positive the north face, (X). Right panel: CIRS-retrieved ring's temperature during 7 of the 10 observations considered in this work. From top to bottom the sub-solar latitude, or solar elevation angle, decreases from -23.5° to 2.6° . In some observations, like in (VIII), are shown the data taken across two consecutive radial scans: this explain the differences observed across the C ring.

The seasonal temperature trends measured by VIMS from 2004 to 2010 are shown in Fig. 18 where the variations observed on two 400 km-wide zones taken across A–B–C rings and CD are reported: with the exclusion of some points corresponding to (VII) mosaic (at -13.7° sub-solar latitude) a decrease of the 3.6 μm peak position, and therefore of the temperature, is seen on each region of the rings when the solar elevation angle decreases. For symmetry, we should expect an increase after the equinox, to be verified with more recent datasets. The maximum spectral shift of the 3.6 μm peak position is seen on the inner A ring ($r = 124,900$ – $125,300$ km) where it moves of about 10 nm from about 3.63 μm to 3.53 μm between observations taken in 2004 and 2010.

Without entering in a discussion about ring particles thermal properties, which is beyond the scope of this paper, we want to point out the importance to integrate VIMS results into different thermo-physical models derived from CIRS observations (Spilker et al., 2006; Ferrari and Leyrat, 2006; Morishima et al., 2009). VIMS surface temperature in fact are interesting to better constrain the thermal properties of the particles' outer layer which is very sensitive to the three main contributions of heating: direct solar flux, saturnshine and Saturn's thermal emission on dayside arc of the orbit while only Saturn's thermal emission at $T = 95$ K is active on the nightside arc of the orbit.

6. Detection of organic features

In this section we report about the possible detection of organic material's absorption bands on VIMS ring spectra. As discussed in

Section 3.2, we have evidences that spectral slopes becomes positive (or red) when water ice particles are polluted by chromophores like carbonaceous particles (Cuzzi and Estrada, 1998), complex organics coming from the irradiation of simple hydrocarbons (Johnson et al., 1983; Moore et al., 1983), amorphous silicates (Poulet et al., 2003), iron or hematite submicron grains (Clark et al., 2008), tholins intimately mixed in water ice grains (Poulet et al., 2003; Ciarniello et al., 2011) or combinations of these materials. With the aim to verify the presence of these contaminants we have focused our analysis on the 3.2–3.5 μm spectral range where organic material's absorption bands are located: aromatic hydrocarbons, structured in benzene rings which form polycyclic aromatic hydrocarbons (or PAH), can be recognized thanks to the diagnostic stretch mode at 3.29 μm . The aliphatic material, structured along carbon chains, shows diagnostic features caused by the methylene (CH_2) stretch modes around 3.42–3.52 μm .

The detection of these organic material features is in general very difficult in VIMS rings spectra because the signal to noise (SNR) conditions are very poor in 3.2–3.5 μm range (see Fig. 5) and the spectral resolution similar or lower to the width of these signatures. Since is impossible to perform a reliable identification of any organic features on moderate to high phase observations, we have restricted our analysis on low phase-high signal mosaic (X) which, despite the short integration time (80 ms) has the highest SNR in the 3.2–3.5 μm spectral range among all observations considered in our analysis (see Figs. 4 and 5).

In the resulting A, B, C rings and CD reflectance spectra, shown in Fig. 19, is possible to recognize the faint absorptions centered at 3.42 and at 3.52 μm arising from the symmetric and asymmetric

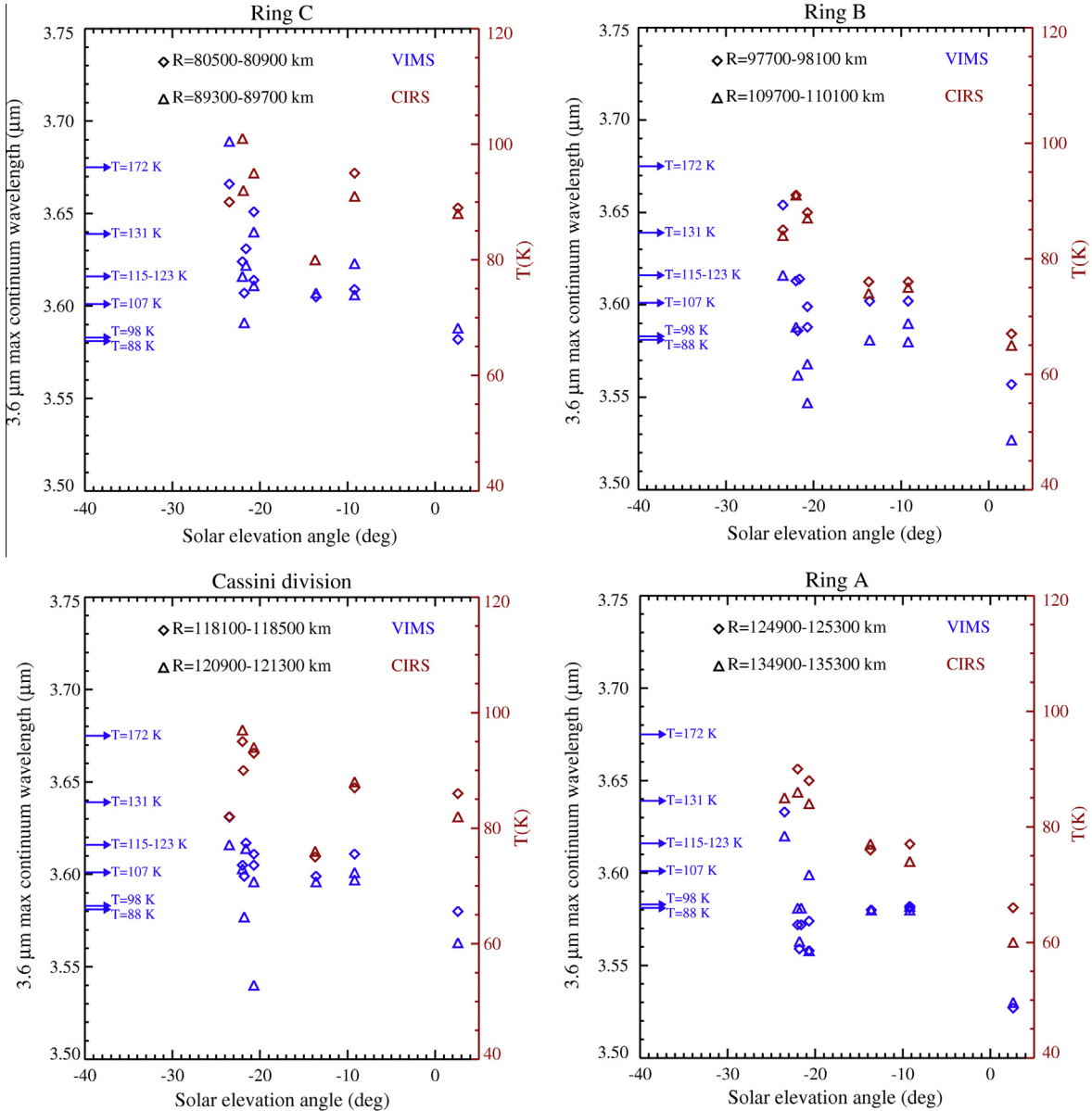


Fig. 18. Seasonal changes of the 3.6 μm maximum continuum wavelength measured by VIMS (blue points). Blue arrows indicate the corresponding temperature scale for pure water ice. CIRS-derived temperature points are in red. From top left to bottom right panels two different 400 km-wide radial positions taken on C, B, CD and A rings are sampled between -23.5° to 2.6° solar elevation angles. (For interpretation of the references to color in this figure legend, the reader is referred to the web version of this article.)

stretch of CH_2 in aliphatic hydrocarbons, respectively (Cruikshank et al., 2008). The 3.29 μm polycyclic aromatic hydrocarbons signature is not evident on these VIMS spectra.

For a more accurate analysis of the features we have normalized the spectra to the local continuum calculated through a 3rd-degree least-square polynomial fit between 3.26 and 3.58 μm. The resulting spectra, shown in Fig. 20 indicate that the two aliphatic features at 3.42 and 3.52 μm are persistent across the entire ring system. The PAH feature at 3.29 μm is much less obvious to detect: this is a consequence of the removal of the continuum, affected by the presence of the relatively strong 3.1 μm peak's shoulder at shorter wavelengths or by the intrinsic weakness of the band.

For the two aliphatic features we have measured the radial profile of the 3.42 and 3.52 μm band depths which are shown in Fig. 21. The 3.42 μm band shows a significant increase in the inner part of the C ring, up to about 0.08. A second maximum at 0.06 is measured on the CD. Across A and B rings the band depth is in

average about 0.03 and never negative. This is an indication that the absorption feature is detected also where the signal is low. The radial distribution of the 3.42 μm band depth has similarities with the $S_{0.55-0.95}$ spectral slope shown in Fig. 8. The 3.52 μm band depth is more uniform and equal to about 0.03 across the entire ring system.

VIMS data show an increase of the 3.42 μm band depth of about 2–3 times across the C ring with respect to the B ring. This is a confirmation of the results reported by Poulet et al. (2003) which have detected the presence of the 3.4 μm aliphatic feature in the ratio of average C/B ring spectra, as a result of enrichment of the aliphatic compound on the C ring.

Conversely, the PAH aromatic feature at 3.29 μm, detected by VIMS on the dark material units of Iapetus leading hemisphere, Phoebe and Hyperion (Cruikshank et al., 2008; Coradini et al., 2008; Clark et al., 2008, 2012; Tosi et al., 2010; Dalton et al., 2012; Dalle Ore et al., 2012), seems to be very faint on C rings

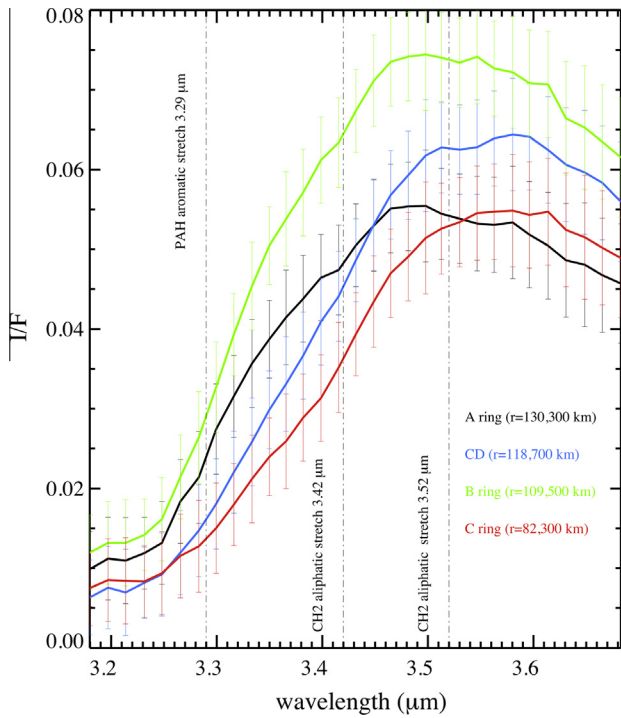


Fig. 19. Average reflectance spectra showing the two aliphatic hydrocarbon absorption features at 3.42–3.52 μm on A, B, C rings and CD. Error bars on reflectances correspond to the 3 sigma level.

and CD spectra and difficult to detect on A and B rings due to the proximity of the relatively strong 3.1 μm Fresnel peak. These properties of the organic features could help us to trace the origin of the chromophores observed in the Saturn's system. In fact, a similar prevalence of the aliphatic bond outnumbering the aromatic component is frequently observed, from interstellar to interplanetary scale distances (Pendleton and Allamandola, 2002). This is the case

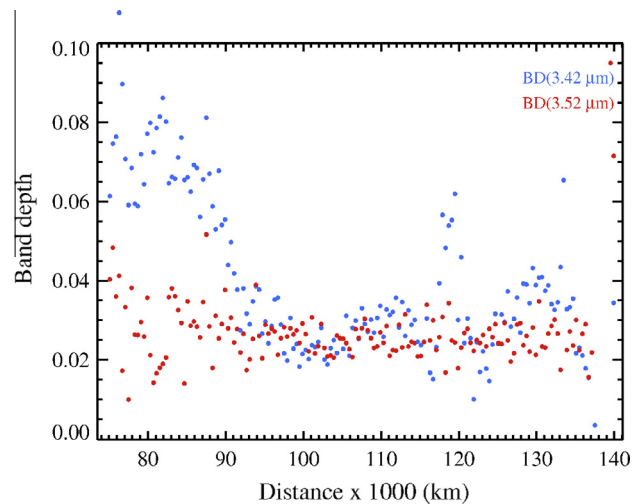


Fig. 21. Radial profile of the aliphatic hydrocarbon band depths at 3.42–3.52 μm .

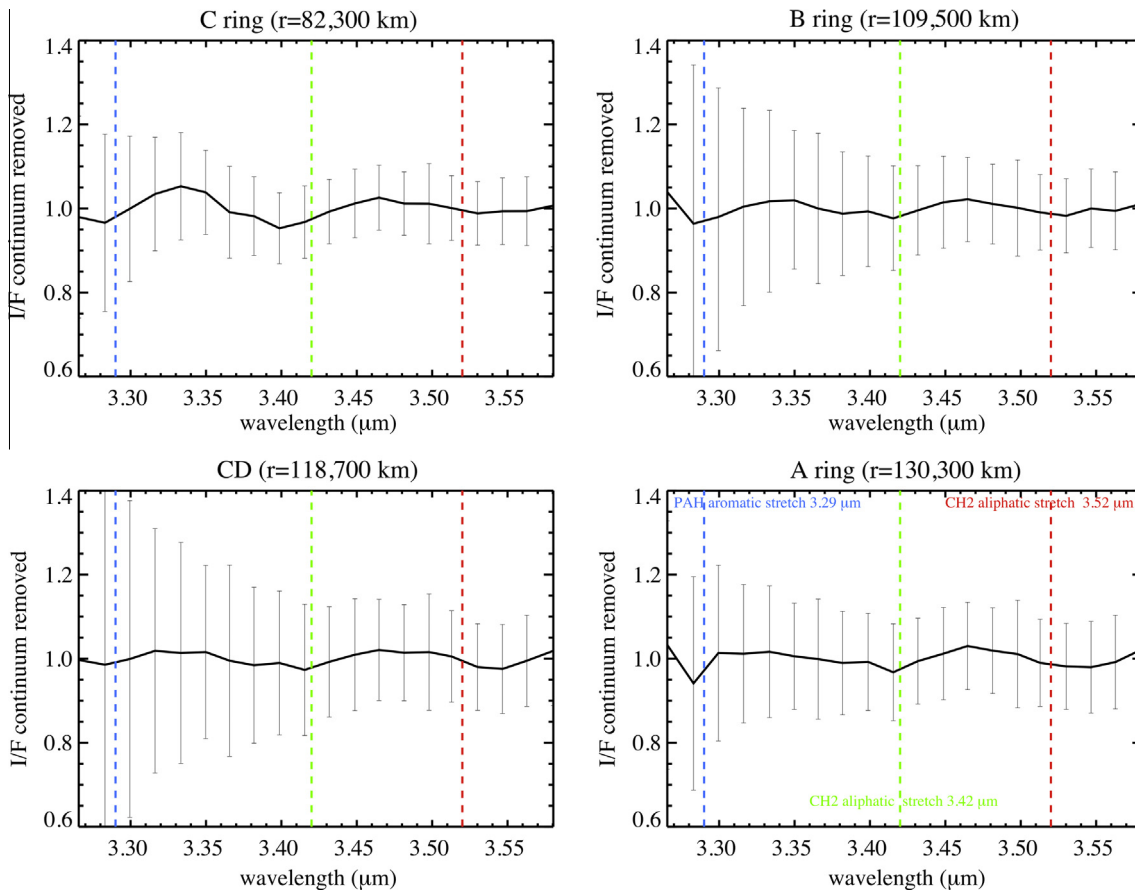


Fig. 20. Continuum-removed reflectance spectra showing the two aliphatic hydrocarbon absorption features at 3.42–3.52 μm on A, B, C rings and CD. The retrieval of the 3.29 μm signature is influenced by the presence of the nearby Fresnel's peak at 3.1 μm . Error bars on reflectances correspond to the 3 sigma level.

of the diffuse interstellar medium (ISM) towards the active galactic nucleus IRAS 08572+3915 (Dartois et al., 2007) where organic material is associated to hydrogenated amorphous carbon (HAC)-rich dust particles; in comet 81P/Wild 2 samples returned by the Stardust mission (Keller et al., 2006) and in interplanetary dust particles (IDP) (Flynn et al., 2008).

Based on this evidence we can argue that the organic material observed across the Saturn's system can be classified in two separate components: the aliphatic one that prevails across inner rings while the aromatic hydrocarbons component dominates across the outer satellites (Hyperion, Iapetus leading hemisphere, Phoebe). The low level of aliphatic material (band depth at about 0.03) observed in A and B ring particles could be an evidence of their pristine composition (Charnoz et al., 2009). Conversely, low-density rings such as the C ring and the CD are more susceptible to being altered compositionally by meteoroid bombardment (Cuzzi and Estrada, 1998) resulting in a higher concentration of carbonaceous particles and aliphatic material (band depth at about 0.06–0.08).

Apart from those preliminary considerations, further steps are necessary to better investigate the nature and distribution of the organic material features because the ring reflectance between 3.2 and 3.5 μm is affected by water ice amount, grain size and temperature: the strong 3.0 μm water ice band dominates at shorter wavelengths, reducing the reflectance to few percent; the intensity of the reflectance around the 3.6 μm peak is strongly grain size-dependent, as discussed in Section 3.4; finally, the position of the 3.6 μm peak and the slope between 3.2 and 3.6 μm are temperature-dependent (Section 5). In particular is interesting to note in Fig. 19 how much the continuum around the 3.52 μm band changes with the temperature: in fact it is very close to the local maximum on cold A–B rings while it moves on the wing of the strong 3.0 μm water ice band on warmer C ring and CD spectra. This means that to disentangle organic composition from water ice, grain size and temperature is necessary to adopt a radiative transfer model in which these parameters can be simulated for the different rings regions. A similar effort is currently under development and shall be addressed by a next paper (III).

7. Discussion and conclusions

In this paper an extensive sub-set of VIMS rings data, made up of ten radial mosaics for a total of 101,566 VIS–IR spectra returned by VIMS from 2004 to 2010 has been analyzed. After having reduced these hyperspectral data mosaics in radial spectrograms at 400 km spatial resolution, we have obtained a comprehensive view of Saturn's main rings in a variety of illumination and viewing geometries. Taking advantage of a similar dataset, several VIS–IR spectral indicators tailored to determine albedo, visual reddening, water ice abundance, regolith grain size and temperature were applied. Such indicators are measured across the entire radial axis from inner C ring to outer A ring, giving us the possibility to analyze the changes induced by phase angle and elevation angle on each region of the ring system.

7.1. Composition

The distribution and mixing of the chromophores bond in water ice particles is traced thanks the radial profiles shown in Figs. 7–10. The two visible $S_{0.35-0.55}$ – $S_{0.55-0.95}$ spectral slopes profiles show opposite behavior: across the high optical depth A–B rings the $S_{0.35-0.55}$ slope reaches the maximum reddening while the $S_{0.55-0.95}$ slope is minimum. Conversely, the $S_{0.55-0.95}$ slope profile has two maxima across the low optical depth regions, the C ring and the CD, where the $S_{0.35-0.55}$ slope has minimum values. Water ice 1.5–2.0 μm band depths are strongly spatially correlated with the

$S_{0.35-0.55}$ slope, reaching maximum depths across outer B ring and A ring. Since the two spectral slopes are correlated to the amount of chromophores and how these contaminants are mixed with water ice particles, we can infer the composition for the main spectral classes observed:

- **A–B rings:** the high $S_{0.35-0.55}$ slope reddening joined to a more neutral $S_{0.55-0.95}$ slope is compatible with an intraparticle–intra-molecular embedding of UV-blue absorbing chromophores in a very abundant water ice matrix (Nicholson et al., 2008). The high concentration of the water ice is confirmed by the strong 1.5–2.0 μm band depths and high I/F(0.55) (see Fig. 6).
- **C ring–CD:** the high $S_{0.55-0.95}$ slope points to the presence of dark chromophores in areal mixing with water ice particles. These two regions appear much darker than A–B rings as a consequence of the low optical depth and of the presence of a larger fraction of dark material dispersed among ice grains (Hedman et al., 2013).

The general compositional properties of the ring's particles as derived from VIMS observations are in agreement with the compositional trend foreseen by the ballistic transport model (Cuzzi and Estrada, 1998) in which dark material, residuum of meteoritic and cometary bombardment on the ring plane, concentrate where optical depth is lower.

7.2. Regolith grain size

Two different methods, based on the comparison of the 2.0 μm band depth (Fig. 10) and I/F(3.6) / I/F(1.8) ratio (Fig. 11) with pure water ice laboratory spectra, were applied. The resulting grain sizes for A–B–C rings and CD are summarized here:

- **A–B rings:** ≈80–100 μm from 2.0 μm band depth; 50–80 μm from I/F(3.6) / I/F(1.8) ratio.
- **C ring:** 20–50 μm from both 2.0 μm band depth and I/F(3.6) / I/F(1.8) ratio.
- **CD:** 50–60 μm from 2.0 μm band depth; <30 μm from I/F(3.6) / I/F(1.8) ratio.

The regolith grain sizes derived by applying these two different spectral indicators converge on very similar results on A, B and C rings. Estimates for C ring and CD could be invalidated by the larger concentration of contaminants. In the past, several attempts were made to estimate the typical size of the water ice particles by using the diagnostic absorption features in the near infrared. The regolith grain size retrieved by Pollack et al. (1973) and Clark and McCord (1980) was in the tens of microns range, similar to the results we have obtained on A–B rings.

7.3. Phase-dependent effects

Both visible spectral slopes (Figs. 12 and 14) and water ice band depth (Figs. 13 and 15) change with the illumination conditions (Veverka et al., 1978; Hapke, 1993): at low and at high phases in addition to the multiple scattering, the opposition surge and the forward scattering effects, respectively, influence the color response of the icy particles. A similar behavior is common for all ring regions, from low density C ring and CD to high density A–B rings. VIMS data confirm the extreme red color of the A–B observed on Voyager data (Estrada and Cuzzi, 1996).

7.4. Regolith temperature

The temperature of the ring particles is derived using the position of the 3.6 μm continuum peak calibrated on crystalline water

ice spectra measured in laboratory (Fig. 16). VIMS data indicate that temperature is anticorrelated with the albedo: low-albedo C ring and CD have higher temperatures than A–B rings where albedo is high. This trend is in agreement with CIRS temperature measurements (Spilker et al., 2013). Since albedo and optical depth are correlated among them across rings, we observe a similar anti-correlation between temperature and optical depth too. Furthermore, with the exception of the CD, the temperature decreases with the distance from Saturn. The availability of data taken at different solar elevation angle allow us to follow how seasonal changes influences the ring's temperature. Mosaics acquired across both solar and antisolar ansae allow us to retrieve the temperature diurnal changes: across the C ring VIMS measures higher temperatures on the solar ansa than on the antisolar one. Finally, comparing co-located VIMS and CIRS temperature measurements performed at the same time (observation II, phase angle 30.7°, solar elevation angle –22°, see Fig. 17) we have seen the following trend across rings:

- *A ring*: VIMS measures $T \approx 105$ K (inner edge) to $T \approx 88$ K (outer edge); CIRS measures $T \approx 90$ K (inner edge) to $T \approx 82$ K (outer edge).
- *B ring*: VIMS measures $T \approx 115$ K (inner edge) to $T \approx 88$ K (outer edge); CIRS measures $T \approx 90$ K (inner edge) to $T \approx 89$ K (outer edge).
- *C ring*: VIMS measures $T \approx 148$ K (inner edge) to $T \approx 115$ K (outer edge); CIRS measures $T \approx 107$ K (inner edge) to $T \approx 90$ K (outer edge).
- *CD*: VIMS peak temperature $T \approx 115$ K; CIRS peak temperature $T \approx 100$ K.

C ring and CD temperatures measured by VIMS through the 3.6 μm peak position method are in general much higher than corresponding ones reported by CIRS (Altobelli et al., 2008; Leyrat et al., 2008; Spilker et al., 2013). Deviation from pure water ice composition and different skindepth sampled by the two instruments are possible causes of these deviations. Conversely, the two instruments give similar results on the outer regions of the A–B rings.

7.5. Organic material

We report the detection of faint features associated with organic material on low phase–high SNR observations. In particular the spectral signature of the aliphatic compounds at 3.42 μm appears stronger on CD and C ring than on A–B rings, in agreement with the results reported by Poulet et al. (2003). The PAH aromatic feature at 3.29 μm , detected by VIMS on the dark material units of Iapetus leading hemisphere, Phoebe and Hyperion is not evident on rings spectra. Based on these results out of the way we speculate that the organic material observed across the Saturn's system can be classified into two separate components: the aliphatic component prevailing across inner rings while the aromatic hydrocarbons component dominates on the outer satellites surfaces.

7.6. Future works

We plan to follow the investigation exposed in this work in two other successive papers. Paper II, led by M. Ciarniello, shall be devoted to the spectral modeling of ring particles by using a Monte Carlo raytracing simulation applied to particulate media. A description of the method we plan to exploit is given in Ciarniello et al. (2014). Paper III, led by D. Cruikshank and C. Dalle Ore will investigate the spectral properties and radial distribution of the organic compounds detected in 3.2–3.5 μm spectral range

using the same data clustering technique employed in Dalle Ore et al. (2012).

Acknowledgments

The authors thank Larry W. Esposito and Cecile Ferrari for the useful comments which improved the quality of the paper. This research has made use of NASA's Astrophysics Data System and was completed thanks to the financial support of the Italian Space Agency (grant I/015/09/0) and NASA through the Cassini project.

References

- Altobelli, N., Spilker, L.J., Leyrat, C., Pilorz, S., 2008. Thermal observations of Saturn's main rings by Cassini CIRS: Phase, emission and solar elevation dependence. *Planet. Space Sci.* 56, 134–146. <http://dx.doi.org/10.1016/j.pss.2007.05.029>.
- Bradley, E.T., Colwell, J.E., Esposito, L.W., 2013. Scattering properties of Saturn's rings in the far ultraviolet from Cassini UVIS spectra. *Icarus* 225, 726–739. <http://dx.doi.org/10.1016/j.icarus.2013.04.008>.
- Brown, R.H. et al., 2004. The Cassini Visual and Infrared Mapping Spectrometer (VIMS) investigation. *Space Sci. Rev.* 115 (1–4), 111–168. <http://dx.doi.org/10.1007/s11214-004-1453-x>.
- Brown, R.H. et al., 2006. Composition and physical properties of Enceladus' surface. *Science* 311, 1425–1428. <http://dx.doi.org/10.1126/science.1121031>.
- Charnoz, S., Dones, L., Esposito, L.W., Estrada, P.R., Hedman, M.M., 2009. Origin and evolution of Saturn's ring system. In: Dougherty, M.K., Esposito, L.W., Krimigis, S.M. (Eds.), *Saturn from Cassini–Huygens*. Springer, Berlin, pp. 537–576. http://dx.doi.org/10.1007/978-1-4020-9217-6_17.
- Ciarniello, M., Capaccioni, F., Filacchione, G., Clark, R.N., Cruikshank, D.P., Cerroni, P., Coradini, A., Brown, R.H., Buratti, B.J., Tosi, F., Stephan, K., 2011. Hapke modeling of Rhea surface properties through Cassini–VIMS spectra. *Icarus* 214, 541–555. <http://dx.doi.org/10.1016/j.icarus.2011.05.010>.
- Ciarniello, M., Capaccioni, F., Filacchione, G., 2012. VIMS Observations of Saturn's Rings Investigated by means of Monte Carlo Ray Tracing. *American Astronomical Society, DPS meeting*, 44, 511.01.
- Ciarniello, M., Capaccioni, F., Filacchione, G., 2013. Testing the Hapke model by means of Monte Carlo ray-tracing. *European Planetary Science Congress 2013*, held 8–13 September in London, UK. <<http://meetings.copernicus.org/epsc2013>>, id.EPSC2013-318.
- Ciarniello, M., Capaccioni, F., Filacchione, G., 2014. A test of the Hapke's model by means of Monte Carlo ray-tracing. *Icarus* 237, 293–305. <http://dx.doi.org/10.1016/j.icarus.2014.04.045>.
- Clark, R.N., Lucey, P.G., 1984. Spectral properties of ice–particulate mixtures and implications for remote sensing. I – Intimate mixtures. *J. Geophys. Res.* 89, 6341–6348. <http://dx.doi.org/10.1029/JB089JB07p06341>.
- Clark, R.N., McCord, T.B., 1980. The rings of Saturn New infrared reflectance measurements and a 0.326–4.08 micron summary. *Icarus* 43, 161–168.
- Clark, R.N., Curchin, J.M., Jaumann, R., Cruikshank, D.P., Brown, R.H., Hoefen, T.M., Stephan, K., Moore, J.M., Buratti, B.J., Baines, K.H., Nicholson, P.D., Nelson, R.M., 2008. Compositional mapping of Saturn's satellite Dione with Cassini VIMS and implications of dark material in the Saturn system. *Icarus* 193, 372–386. <http://dx.doi.org/10.1016/j.icarus.2007.08.035>.
- Clark, R.N., Cruikshank, D.P., Jaumann, R., Brown, R.H., Curchin, J.M., Hoefen, T.D., Stephan, K., Buratti, B.J., Filacchione, G., Baines, K.H., Nicholson, P.D., 2012. The composition of Iapetus: Mapping results from Cassini VIMS. *Icarus* 218, 831–860. <http://dx.doi.org/10.1016/j.icarus.2012.01.008>.
- Colwell, J.E., Esposito, L.W., Sremcevic, M., 2006. Self-gravity wakes in Saturn's A ring measured by stellar occultations from Cassini. *Geophys. Res. Lett.* 33, 7201.
- Coradini, A. et al., 2004. Cassini/VIMS-V at Jupiter: Radiometric calibration test and data results. *Planet. Space Sci.* 52 (7), 661–670. <http://dx.doi.org/10.1016/j.pss.2003.11.005>.
- Coradini, A., Tosi, F., Gavrinish, A.I., Capaccioni, F., Cerroni, P., Filacchione, G., Adriani, A., Brown, R.H., Bellucci, G., Formisano, V., D'Aversa, E., Lunine, J.I., Baines, K.H., Bibring, J.-P., Buratti, B.J., Clark, R.N., Cruikshank, D.P., Combes, M., Drossart, P., Jaumann, R., Langevin, Y., Matson, D.L., McCord, T.B., Mennella, V., Nelson, R.M., Nicholson, P.D., Sicardy, B., Sotin, C., Hedman, M.M., Hansen, G.B., Hibbitts, C.A., Showalter, M., Griffith, C., Strazzulla, G., 2008. Identification of spectral units on Phoebe. *Icarus* 193, 233–251. <http://dx.doi.org/10.1016/j.icarus.2007.07.023>.
- Cruikshank, D.P., Wegryn, E., Dalle Ore, C.M., Brown, R.H., Bibring, J.-P., Buratti, B.J., Clark, R.N., McCord, T.B., Nicholson, P.D., Pendleton, Y.J., Owen, T.C., Filacchione, G., Coradini, A., Cerroni, P., Capaccioni, F., Jaumann, R., Nelson, R.M., Baines, K.H., Sotin, C., Bellucci, G., Combes, M., Langevin, Y., Sicardy, B., Matson, D.L., Formisano, V., Drossart, P., Mennella, V., 2008. Hydrocarbons on Saturn's satellites Iapetus and Phoebe. *Icarus* 193, 334–343. <http://dx.doi.org/10.1016/j.icarus.2007.04.036>.
- Cruikshank, D.P., Meyer, A.W., Brown, R.H., Clark, R.N., Jaumann, R., Stephan, K., Hibbitts, C.A., Sandford, S.A., Mastrapa, R.M.E., Filacchione, G., Ore, C.M.D., Nicholson, P.D., Buratti, B.J., McCord, T.B., Nelson, R.M., Dalton, J.B., Baines, K.H., Matson, D.L., 2010. Carbon dioxide on the satellites of Saturn: Results from the

- Cassini VIMS investigation and revisions to the VIMS wavelength scale. *Icarus* 206, 561–572. <http://dx.doi.org/10.1016/j.icarus.2009.07.012>.
- Cuzzi, J.N., Durisen, R.H., 1990. Meteoroid bombardment of planetary rings: General formulation and effects of Oort cloud projectiles. *Icarus* 84, 467–501.
- Cuzzi, J.N., Estrada, P.R., 1998. Compositional evolution of Saturn's rings due to meteoroid bombardment. *Icarus* 132, 1–35.
- Cuzzi, J.N. et al., 1984. Saturn's rings – Properties and processes. In: Greenberg, R., Brahic, A. (Eds.), *Planetary Rings*. University of Arizona Press, Tucson, pp. 73–199.
- Cuzzi, J.N., French, R.G., Dones, L., 2002. HST multicolor (255–1042 nm) photometry of Saturn's main rings. I: Radial profiles, phase and opening angle variations, and regional spectra. *Icarus* 158, 199–223.
- Cuzzi, J.N. et al., 2009. Ring particle composition and size distribution. In: Dougherty, M.K., Esposito, L.W., Krimigis, S.M. (Eds.), *Saturn from Cassini-Huygens*. Springer, Berlin, pp. 459–509, http://dx.doi.org/10.1007/978-1-4020-9217-6_15.
- Cuzzi, J.N. et al., 2010. An evolving view of Saturn's dynamic rings. *Science* 327 (5972), 1470–1475. <http://dx.doi.org/10.1126/science.1179118>.
- Dalle Ore, C.M., Cruikshank, D.P., Clark, R.N., 2012. Infrared spectroscopic characterization of the low-albedo materials on Iapetus. *Icarus* 221, 735–743. <http://dx.doi.org/10.1016/j.icarus.2012.09.010>.
- Dalton, J.B., Cruikshank, D.P., Clark, R.N., 2012. Compositional analysis of Hyperion with the Cassini Visible and Infrared Mapping Spectrometer. *Icarus* 220, 752–776. <http://dx.doi.org/10.1016/j.icarus.2012.05.003>.
- Dartois, E. et al., 2007. IRAS 08572+3915: Constraining the aromatic versus aliphatic content of interstellar HACs. *Astron. Astrophys.* 463, 635–640. <http://dx.doi.org/10.1051/0004-6361:20066572>.
- D'Aversa, E. et al., 2010. The spectrum of a Saturn ring spoke from Cassini/VIMS. *Geophys. Res. Lett.* 37, L01203. <http://dx.doi.org/10.1029/2009GL041427>.
- Dones, L., Cuzzi, J.N., Showalter, M.R., 1993. Voyager photometry of Saturn's A ring. *Icarus* 105, 184–215.
- Esposito, L.W., 1979. Extensions to the classical calculation of the effect of mutual shadowing in diffuse reflection. *Icarus* 39, 69–80. [http://dx.doi.org/10.1016/0019-1035\(79\)90101-5](http://dx.doi.org/10.1016/0019-1035(79)90101-5).
- Estrada, P.R., Cuzzi, J.N., 1996. Voyager observations of the color of Saturn's rings. *Icarus* 122, 251–272.
- Ferrari, C., Leyrat, C., 2006. Thermal emission of spherical spinning ring particles: The standard model. *Astron. Astrophys.* 447, 745–760.
- Filacchione, G., 2006. Calibrazioni a terra e prestazioni in volo di spettrometri ad immagine nel visibile e nel vicino infrarosso per le sperimentazioni planetarie (On-ground calibrations and in flight performances of VIS-NIR imaging spectrometers for planetary exploration). PhD dissertation, Università degli studi di Napoli Federico II. ftp://ftp.iasf-roma.inaf.it/gianrico/phd/Filacchione_PHD_2006.pdf (in Italian).
- Filacchione, G., Capaccioni, F., McCord, T.B., Coradini, A., Cerroni, P., Bellucci, G., Tosi, F., D'Aversa, E., Formisano, V., Brown, R.H., Baines, K.H., Bibring, J.P., Buratti, B.J., Clark, R.N., Combes, M., Cruikshank, D.P., Drossart, P., Jaumann, R., Langevin, Y., Matson, D.L., Mennella, V., Nelson, R.M., Nicholson, P.D., Sicardy, B., Sotin, C., Hansen, G., Hibbitts, K., Showalter, M., Newman, S., 2007. Saturn's icy satellites investigated by Cassini-VIMS. I. Full-disk properties: 350–5100 nm reflectance spectra and phase curves. *Icarus* 186, 259–290. <http://dx.doi.org/10.1016/j.icarus.2006.08.001>.
- Filacchione, G., Capaccioni, F., Clark, R.N., Cuzzi, J.N., Cruikshank, D.P., Coradini, A., Cerroni, P., Nicholson, P.D., McCord, T.B., Brown, R.H., Buratti, B.J., Tosi, F., Nelson, R.M., Jaumann, R., Stephan, K., 2010. Saturn's icy satellites investigated by Cassini-VIMS. II. Results at the end of nominal mission. *Icarus* 206, 507–523. <http://dx.doi.org/10.1016/j.icarus.2009.11.006>.
- Filacchione, G., Capaccioni, F., Ciarniello, M., Clark, R.N., Cuzzi, J.N., Nicholson, P.D., Cruikshank, D.P., Hedman, M.M., Buratti, B.J., Lunine, J.I., Soderblom, L.A., Tosi, F., Cerroni, P., Brown, R.H., McCord, T.B., Jaumann, R., Stephan, K., Baines, K.H., Flamini, E., 2012. Saturn's icy satellites and rings investigated by Cassini-VIMS: III – Radial compositional variability. *Icarus* 220, 1064–1096. <http://dx.doi.org/10.1016/j.icarus.2012.06.040>.
- Filacchione, G. et al., 2013. The radial distribution of water ice and chromophores across Saturn's system. *Astrophys. J.* 776, 76. <http://dx.doi.org/10.1088/0004-637X/776/2/76>.
- Flasar, F.M. et al., 2004. Exploring the Saturn system in the thermal infrared: The composite infrared spectrometer. *Space Sci. Rev.* 115, 169–297. <http://dx.doi.org/10.1007/s11214-004-1454-9>.
- Flynn, G.J., Keller, L.P., Wirick, S., Jacobsen, C., 2008. Organic matter in interplanetary dust particles. In: Kwok, S., Sandford, S. (Eds.), *Organic Matter in Space*, Proceedings IAU Symposium, vol. 251, pp. 267–276. <http://dx.doi.org/10.1017/S174392130802173X>.
- French, R.G., Salo, H., McGhee, C.A., Dones, L., 2007. HST observations of azimuthal asymmetry in Saturn's rings. *Icarus* 189, 493–522.
- Grundy, W.M., Schmitt, B., 1998. The temperature-dependent near-infrared absorption spectrum of hexagonal H_2O ice. *J. Geophys. Res.* 103 (E11), 25809–25822.
- Hanel, R. et al., 1982. Infrared observations of the saturnian system from Voyager 2. *Science* 215, 544–548.
- Hapke, B., 1993. *Theory of Reflectance and Emittance Spectroscopy*. Cambridge Univ. Press, Cambridge, UK.
- Hedman, M.M. et al., 2007. Self-gravity wake structures in Saturn's A ring revealed by Cassini VIMS. *Astron. J.* 133, 2624–2629.
- Hedman, M.M., Nicholson, P.D., Cuzzi, J.N., Clark, R.N., Filacchione, G., Capaccioni, F., Ciarniello, M., 2013. Correlations between spectra and structure in Saturn's main rings. *Icarus* 223, 105–130. <http://dx.doi.org/10.1016/j.icarus.2012.10.014>.
- Jaumann, R. et al., 2006. High-resolution Cassini-VIMS mosaics of Titan and the icy saturnian satellites. *Planet. Space Sci.* 54, 1146–1155. <http://dx.doi.org/10.1016/j.pss.2006.05.034>.
- Johnson, R.E., Lanzerotti, L.J., Brown, W.L., Augustyniak, W.M., Mussel, C., 1983. Charged particle erosion of frozen volatiles in ice grains and comets. *Astron. Astrophys.* 123, 343–346.
- Keller, L.P. et al., 2006. Infrared spectroscopy of Comet 81P/Wild 2 samples returned by Stardust. *Science* 314 (5806), 1728. <http://dx.doi.org/10.1126/science.1135796>.
- Kuiper, G.P., Cruikshank, D.P., Fink, U., 1970. The composition of Saturn's rings. *Sky Telescope* 39, 14.
- Kunde, V. et al., 1996. Cassini infrared Fourier spectroscopic investigation. *SPIE Proc.* 2803, 162–177.
- Lebofsky, L.A., Johnson, T.V., McCord, T.B., 1970. Saturn's rings: Spectral reflectivity and compositional implications. *Icarus* 13, 226–230.
- Leyrat, C., Spilker, L.J., Altobelli, N., Pilorz, S., Ferrari, C., 2008. Infrared observations of Saturn's rings by Cassini CIRS: Phase angle and local time dependence. *Planet. Space Sci.* 56, 117–133. <http://dx.doi.org/10.1016/j.pss.2007.04.020>.
- Marouf, E.A. et al., 2006. Structure and properties of Saturn's Ring B from Cassini radio occultations. *Bull. Am. Astron. Soc.* 38, 552.
- Mastranza, R.M., Sandford, A.A., Roush, T.L., Cruikshank, D.P., Dalle Ore, C.M., 2009. Optical constants of amorphous and crystalline H_2O -ice: 2.5–22 μm (4000–455 cm^{-1}) optical constants of H_2O -ice. *Astrophys. J.* 701, 1347–1356. <http://dx.doi.org/10.1088/0004-637X/701/2/1347>.
- McCord, T.B., Coradini, A., Hibbitts, C.A., Capaccioni, F., Hansen, G.B., Filacchione, G., Clark, R.N., Cerroni, P., Brown, R.H., Baines, K.H., Bellucci, G., Bibring, J.-P., Buratti, B.J., Bussolletti, E., Combes, M., Cruikshank, D.P., Drossart, P., Formisano, V., Jaumann, R., Langevin, Y., Matson, D.L., Nelson, R.M., Nicholson, P.D., Sicardy, B., Sotin, C., 2004. Cassini-VIMS observations of the Galilean satellites including the VIMS calibration procedure. *Icarus* 172, 104–126. <http://dx.doi.org/10.1016/j.icarus.2004.07.001>.
- Moore, M.H., Donn, B., Khanna, R., A'Hearn, M.F., 1983. Studies of proton-irradiated cometary-type ice mixtures. *Icarus* 54, 388–405. [http://dx.doi.org/10.1016/0019-1035\(83\)90236-1](http://dx.doi.org/10.1016/0019-1035(83)90236-1).
- Morishima, R., Salo, H., Ohtsuki, K., 2009. A multilayer model for thermal infrared emission of Saturn's rings: Basic formulation and implications for Earth-based observations. *Icarus* 201, 634–654. <http://dx.doi.org/10.1016/j.icarus.2009.01.019>.
- Nicholson, P.D., Hedman, M.M., Clark, R.N., Showalter, M.R., Cruikshank, D.P., Cuzzi, J.N., Filacchione, G., Capaccioni, F., Cerroni, P., Hansen, G.B., Sicardy, B., Drossart, P., Brown, R.H., Buratti, B.J., Baines, K.H., Coradini, A., 2008. A close look at Saturn's rings with Cassini VIMS. *Icarus* 193, 182–212. <http://dx.doi.org/10.1016/j.icarus.2007.08.036>.
- Pendleton, Y.J., Allamandola, L.J., 2002. The organic refractory material in the diffuse interstellar medium: Mid-infrared spectroscopic constraints. *Astrophys. J. Suppl.* 138, 75–98. <http://dx.doi.org/10.1086/322999>.
- Pilcher, C.B., Chapman, C.R., Lebofsky, L.A., Kieffer, H.H., 1970. Saturn's rings: Identification of water frost. *Science* 167, 1372–1373.
- Pollack, J.B., Summers, A.L., Baldwin, B.J., 1973. Estimates of the size of the particles in Saturn's rings and their cosmogonic implications. *Icarus* 20, 263–278.
- Porco, C.C. et al., 2006. Cassini observes the active south pole of Enceladus. *Science* 311 (5766), 1393–1401. <http://dx.doi.org/10.1126/science.1123013>.
- Poulet, F., Cuzzi, J.N., 2001. The composition of Saturn's rings. *Icarus* 160, 350–358.
- Poulet, F., Cruikshank, D.P., Cuzzi, J.N., Roush, T.L., French, R.G., 2003. Compositions of Saturn's rings A, B, and C from high resolution near-infrared spectroscopic observations. *Astron. Astrophys.* 412, 305–316. <http://dx.doi.org/10.1051/0004-6361:20031123>.
- Shkuratov, Y., Starukhina, L., Hoffmann, H., Arnold, G., 1999. A model of spectral albedo of particulate surfaces: Implications for optical properties of the Moon. *Icarus* 137, 235–246. <http://dx.doi.org/10.1006/icar.1998.6035>.
- Smith, B.A. et al., 1981. Encounter with Saturn – Voyager 1 imaging science results. *Science* 212, 163–191. <http://dx.doi.org/10.1126/science.212.4491.163>.
- Smith, B.A. et al., 1982. A new look at the Saturn system – The Voyager 2 images. *Science* 215, 504–537. <http://dx.doi.org/10.1126/science.215.4532.504>.
- Spilker, L.J. et al., 2006. Cassini thermal observations of Saturn's main rings: Implications for particle rotation and vertical mixing. *Planet. Space Sci.* 54, 1167–1176. <http://dx.doi.org/10.1016/j.pss.2006.05.033>.
- Spilker, L.J., Ferrari, C., Cuzzi, J.N., Showalter, M., Pearl, J., Wallis, B., 2003. Saturn's rings in the thermal infrared. *Planet. Space Sci.* 51, 929–935. <http://dx.doi.org/10.1016/j.pss.2003.05.004>.
- Spilker, L.J., Ferrari, C., Morishima, R., 2013. Saturn's ring temperatures at equinox. *Icarus* 226, 316–322. <http://dx.doi.org/10.1016/j.icarus.2013.06.002>.
- Tamayo, D., Burns, J.A., Hamilton, D.P., Hedman, M.M., 2011. Finding the trigger to Iapetus' odd global albedo pattern: Dynamics of dust from Saturn's irregular satellites. *Icarus* 215, 260–278. <http://dx.doi.org/10.1016/j.icarus.2011.06.027>.
- Thompson, W.T., Lumme, K., Irvine, W.M., Baum, W.A., Esposito, L.W., 1981. Saturn's rings – Azimuthal variations, phase curves, and radial profiles in four colors. *Icarus* 46, 187–200.

- Tosi, F., Turrini, D., Coradini, A., Filacchione, G., 2010. Probing the origin of the dark material on Iapetus. *Mon. Not. R. Astron. Soc.* 403, 1113–1130. <http://dx.doi.org/10.1111/j.1365-2966.2010.16044.x>.
- Vahidinia, S., Cuzzi, J.N., Hedman, M.M., Draine, B., Clark, R.N., Roush, T., Filacchione, G., Nicholson, P.D., Brown, R.H., Buratti, B.J., Sotin, C., 2011. Saturn's F ring grains: Aggregates made of crystalline water ice. *Icarus* 215, 682–694. <http://dx.doi.org/10.1016/j.icarus.2011.04.011>.
- Verbiscer, A.J., Skrutskie, M.F., Hamilton, D.P., 2009. Saturn's largest ring. *Nature* 461, 1098–1100. <http://dx.doi.org/10.1038/nature08515>.
- Verkerk, J., Goguen, J., Yang, S., Elliot, J., 1978. Scattering of light from particulate surfaces. I – A laboratory assessment of multiple-scattering effects. *Icarus* 34, 406–414. [http://dx.doi.org/10.1016/0019-1035\(78\)90176-8](http://dx.doi.org/10.1016/0019-1035(78)90176-8).